Available online at www.sciencedirect.com
ScienceDirect
Deep-Sea Research II 55 (2008) 1075–1097
DEEP-SEA RESEARCH PART II
www.elsevier.com/locate/dsr2

Physics of early summer ice/ocean exchanges in the western Weddell Sea during ISPOL

Miles G. McPhee*

McPhee Research Company, Naches, WA 98937, USA

Accepted 28 December 2007
Available online 10 April 2008

Abstract

Early summer exchanges of momentum, heat, and salt between a multiyear ice floe and the underlying upper ocean in the western Weddell Sea were investigated during the Ice Station Polarstern (ISPOL) drift. Instrumentation clusters including three-dimensional acoustic current meters, temperature and conductivity meters were deployed at up to three levels beneath two different sites on the ISPOL floe, at depths ranging from 3 to 10 m below the ice/ocean interface. ISPOL presented a complex physical environment with the floe comprising a mixture of ice types, responding to relatively strong tidal and internal ice forcing, drifting in a matrix of rapidly shifting open-water areas. Turbulence measured during the drift was generally moderately energetic during spring tides early and late in the drift, with maximum interfacial stress approaching 0.2 Pa. Measured turbulent heat flux at the instrument levels, which varied from about 20 upward to 70 $W m^{-2}$ downward, responded to both solar radiative and horizontal advective effects, therefore did not necessarily correspond to interface heat flux values. Currents measured with an acoustic Doppler profiler showed consistent Ekman turning in the water column between 10 and 30 m. A novel application of modeling based on temperature and salinity profiles plus relative current measured at 20 m provided an estimate of the representative undersurface hydraulic roughness for the floe: $z_0 = 0.04$ m. By solving the numerical model used to establish z_0 for all 3-h average segments when relative current at 20 m exceeded 0.03 $m s^{-1}$, interface conditions were estimated for the entire drift. Average values evaluated at the ice/water interface included turbulent stress of about 0.05 Pa; turbulent heat flux of about 15 $W m^{-2}$ (implying a maximum bottom ablation of around 15 cm); and salinity flux of about 1.5×10^{-6} psu $m s^{-1}$.

Keywords: Turbulent boundary layer; Reynolds stresses; Eddy conduction; Ekman spiral; Salt flux

1. Introduction

The 2004–2005 *Ice Station Polarstern* (ISPOL) project included a month-long passive drift with the ship moored to an ice floe typical of the multiyear pack of the western Weddell Sea (Hellmer et al., 2008). One facet of the experiment was an upper-ocean physics program designed primarily to characterize the exchange of heat, salt and momentum at the underside of drifting multiyear ice during early summer. These exchanges are thought to play a prominent role in the development of biological and biogeochemical activity within and just below the pack ice (Thomas and Dieckmann, 2003), and to contribute significantly to the energy balance that determines evolution of the ice pack as it drifts north. Because of its geographic proximity to the 1992 drift of Ice Station Weddell (ISW) (Gordon et al., 1993) ISPOL provided a useful supplement and contrast to ice/ocean exchanges observed at ISW in early winter (McPhee and Martinson, 1994; McPhee, 1994; Robertson et al., 1995). Among the ISW findings, was evidence that at least during storms when the ice was predominantly wind driven, ocean boundary layer (OBL) turbulence could be described by a relatively simple similarity treatment of the neutral eddy exchange coefficients (McPhee and Martinson, 1994). Robertson et al. (1995) used microstructure measurements and double-diffusion arguments to show that the upward

*Tel./fax: +1 509 658 2575.
E-mail addresses: mmcphee@starband.net, miles@apl.washington.edu.

0967-0645/$ - see front matter © 2008 Elsevier Ltd. All rights reserved.
doi:10.1016/j.dsr2.2007.12.022

flux of heat in the pycnocline was modest (averaging about $2\,W\,m^{-2}$), and that this matched within about 15% the average upward heat flux in the OBL estimated from a bulk parameterization proportional to product of mean elevation of mixed layer temperature above freezing (δT) and interface friction velocity following McPhee (1992).

Summer data from Arctic ice-drift projects also provide an interesting counterpoint to the ISPOL measurements, since they too come from multiyear pack ice at high latitudes. A notable feature of the Surface Heat Budget of the Arctic (SHEBA) measurements during June of 1998 was a rapid increase in basal heat flux from about $5\,W\,m^{-2}$ at the first of the month to around $15\,W\,m^{-2}$ by July 1 (Perovich and Elder, 2002). Similar increases were seen at the AIDJEX stations in the 1970s and more recently in data from the North Pole Environmental Observatory unmanned buoys (McPhee et al., 2003). The increases corresponded to increasing δT as mixed layer temperature increased in response to solar heating through leads and thin ice. At SHEBA, there was often a fairly pronounced diurnal cycle in mixed layer temperature during June, accompanied by downward heat flux near local noon (McPhee et al., 2001).

This paper presents upper-ocean current, temperature, and salinity measurements made during the ISPOL drift, using instrumentation systems capable of measuring at time and spatial scales small enough to capture the "energy containing" part of the turbulence spectrum, hence accurate estimates of local turbulent fluxes. Compared with most previous studies of the under-ice OBL, ISPOL presented a complex physical environment, with a very heterogeneous ice morphology, relatively strong tidal forcing, rapidly shifting open-water areas nearby (during a time of intense shortwave radiation), and significant ice deformation. It became apparent as the analysis progressed that often the "local" turbulence measurements were representative of a relatively limited surrounding area, highly dependent on both flow direction and measurement depth. Consequently, the approach taken here is to combine the data with simple modeling concepts to seek a more general description, representative of the entire floe (and presumably surrounding floes). The fields thus described include: turbulent stress, heat flux, and salt flux at the ice/ocean interface, plus profiles of velocity in the OBL along with estimates of geostrophic surface current. In addition, we present estimates of eddy viscosity and scalar diffusivity, with the hope that these may prove useful to others investigating, e.g., nutrient, dissolved gas, or biota distributions in the ice/upper-ocean system.

2. Physical description

2.1. Apparatus

Instrumentation for the ISPOL upper-ocean physics program included both *turbulence instrument clusters* (TICs) and acoustic Doppler profilers (ADPs), deployed through hydroholes made by drilling and sawing at locations on the floe far enough from the ship to minimize flow or thermodynamic disturbance from the R.V. *Polarstern*. Two sites (Ocean Turbulence I and II, OT-I and OT-II) were used during the project. The first was occupied from 30 November to 25 December 2004 in 2-m-thick ice (with ~1 m snow initially) roughly 300 m off R.V. *Polarstern's* port bow. Power was supplied by electrical cable from the ship, which also served the nearby meteorological site. After the floe breakup and relocation to the largest remnant of the original floe on Christmas day, the project was relocated to relatively thinner ice (1 m thick) near the end of a snow survey line. Power at OT-II was supplied by portable generator.

The original experiment design called for a mast made from stainless-steel rods approximately 7 m in length that could be lowered to variable depths in the upper ocean. The mast included two TICs, mounted 4 m apart, and two ADPs: one RDI 1.2 MHz Workhorse ADCP mounted to look upward from near the bottom of the mast, and one RDI 5-beam, 0.6-MHz broadband ADCP configured to look down from the base of the mast. Each TIC included a Sontek 5 MHz, ADVOcean 3-axis acoustic Doppler velocimeter, plus SBE 03 temperature and SBE 04 conductivity sensors. One TIC included an SBE 07 microstructure conductivity (μC) sensor. Probes for the temperature and μC sensors were mounted in the same horizontal plane as the measurement volume of the ADV (a roughly 1×2 cm ellipsoid centered 18 cm from the transducer sound source), offset so as to prevent interference with the current measurements. All of the instruments described above, plus a SBE 50 pressure sensor were interfaced to a custom Sea-Bird SBE 9+ CTD, utilizing five standard frequency channels, five voltage channels (1 for pressure, 4 for one ADV), the standard RS232 serial uplink (for the other ADV), plus a second RS422 serial channel through which the data streams for both of the RDI instruments were multiplexed. In addition to the beam velocity data, the RDI instrument streams included compass and tilt information. Output from the SBE 11+ deck unit was fed in three serial channels to a Linux-based laptop computer, and recorded.

A second SBE 911+ system comprising one TIC plus a Sontek 0.5 MHz acoustic Doppler profiler was brought as a backup. After the initial setup, it was also deployed, first on its own separate mast, then later combined with the primary mast to furnish three instrument clusters for most of the OT-I deployment. After the Christmas breakup, one mast with two TICs and the 0.5 MHz Sontek ADP were deployed for OT-II.

The original TIC concept (using mechanical current meters) has been in use for about two decades and is well documented (see, e.g., McPhee et al., 1987; McPhee, 1994, 2002). Since the 1997–1998 SHEBA project, the mechanical current meters have been replaced by ADVOcean acoustic current meters, as described, e.g., by Fer et al. (2004).

2.2. Ice station drift velocity

A continuous record of ice velocity, necessary for determining absolute current velocities from instruments deployed from the drifting floe, was obtained using 5-min averages of ship GPS positions, made available on the ship network in near real time. For each drift station segment (i.e. before and after the Christmas-day breakup), latitude–longitude pairs were converted to a polarstereographic (ps) grid centered at 67°56′S, 55°56′W, oriented so that the positive y-axis is aligned with north. The positions were then used to estimate velocity by two methods. In the first, all 5-min position vectors in a 1-h time window centered at even half-hour intervals were converted to complex numbers and least-squares fitted to a complex second-order polynomial. The derivative of this numerical function, evaluated by linear interpolation to a particular time, then furnishes an estimate of the complex velocity, which can be rotated into a true east (U) and north (V) vector.

The second method invokes physical arguments about the combined inertia and tidal motion of the coupled ice/upper-ocean system to determine velocity by complex demodulation. The method, described in detail by McPhee (1988), fits all of the data over a 1-day (diurnal period) time window to a position function including mean velocity and clockwise and anticlockwise oscillating components at the

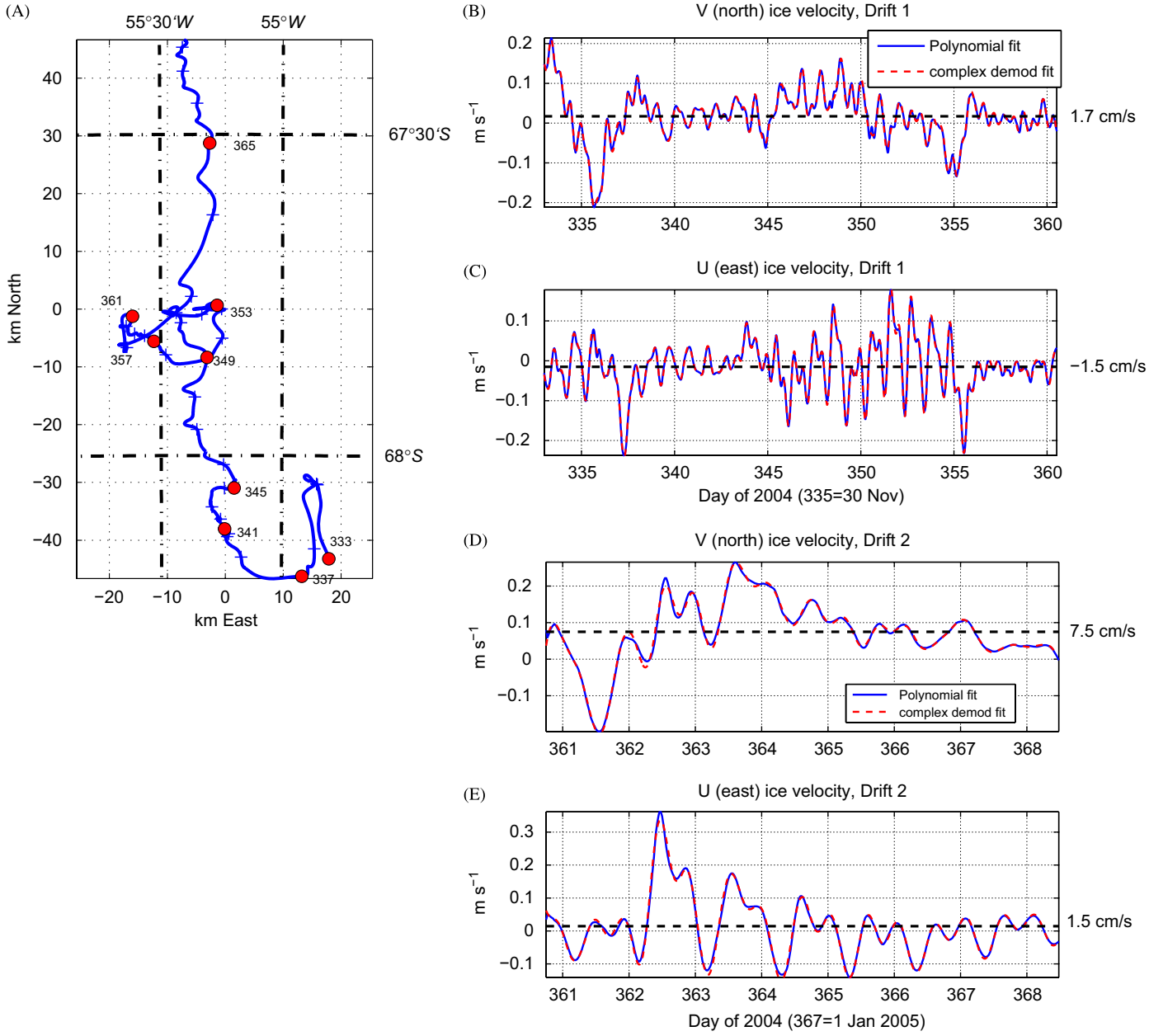

Fig. 1. (A) ISPOL drift trajectory. (B) Northward velocity component, Drift 1 (before Christmas breakup). Two methods were used to calculate velocity from ship positions as described in the text. (C) Same except eastward component. (D) Northward component, Drift 2. (E) Eastward component, Drift 2.

inertial and diurnal frequencies. As with the polynomial procedure, the function coefficients are evaluated at set intervals (90 min), with velocity found by differentiating the interpolated position function at particular times. The complex-demodulation method provides a rational separation of "mean" motion from inertial/semidiurnal and diurnal tidal loops, which were ubiquitous during the ISPOL drift. Velocities calculated by both methods for the Drifts 1 and 2 are compared in Fig. 1. Mean values (dashed horizons) show that the overall drift was quite slow, particularly during Drift 1. Root-mean-square speeds were larger: 7.6 and 12.3 cm s^{-1} during Drifts 1 and 2, respectively, indicating the influence of mixed diurnal and semidiurnal tides.

The comparison between complex demodulation and polynomial fitting techniques shows that the respective velocity estimates differ in rms speeds by less than 7 mm s^{-1}. Complex demodulation provides estimates of the both the semidiurnal (M_2, close enough to inertial that the rms fitted velocities differ by less than 2 mm s^{-1}) and diurnal (K_1) oscillating velocities (shown for Drift 1 in Fig. 2). The rms diurnal tidal signal is about 60% larger than semidiurnal, and there is a clear east—west (offshore–onshore) dominance.

Although the tidal signal in ice motion was qualitatively similar to results from a tidal model of the region (R. Muench, personal comm., 2004), it is not the same as the ocean tide. Pack ice when unconstrained by internal stress gradients often drifts in phase with the upper ocean, and the main driving force for the mean ice motion is wind (e.g., McPhee, 1980). For an observer on the drifting ice (whose instruments are also oscillating in phase with the inertial/tidal signal) currents measured in the upper ocean will thus lack much inertial/tidal signal. This was not the case for ISPOL, where currents measured relative to the ice often had a tidal component. Previous studies of summer drift of ~2-m-thick pack ice in the Arctic (McPhee, 1980, 2002) and winter drift of thin ice in the eastern Weddell (McPhee et al., 1996) have shown strong correlation between ice drift and wind speed, and in the perennial ice pack of the Arctic, this ratio of drift speed (with inertial/tidal oscillations removed) to 10-m wind speed is consistently around 2%, when the ice is freely drifting (McPhee, 1980, 2002). This did not hold for ISPOL (Fig. 3). Although some correlation between drift speed and wind speed is obvious, it was relatively modest (0.66 correlation coefficient), and the overall average ratio was around 1.5% for the wind speed adjusted to the 10-m level (assuming a wind drag coefficient of 0.002). There are also times, notably the period prior to the Christmas breakup (days 355–360), when the wind was relatively strong but mean ice drift was slow, indicating a sizable departure of the ice force balance from free-drift conditions.

2.3. Floe mapping

It became clear as the experiment progressed that characteristics of flow measured at the ocean turbulence site depended, sometimes strongly, on the orientation of the current relative to the geometry of the floe. To this end, the floe was mapped by skiing its perimeter with a handheld GPS device, then subtracting the ship positions at

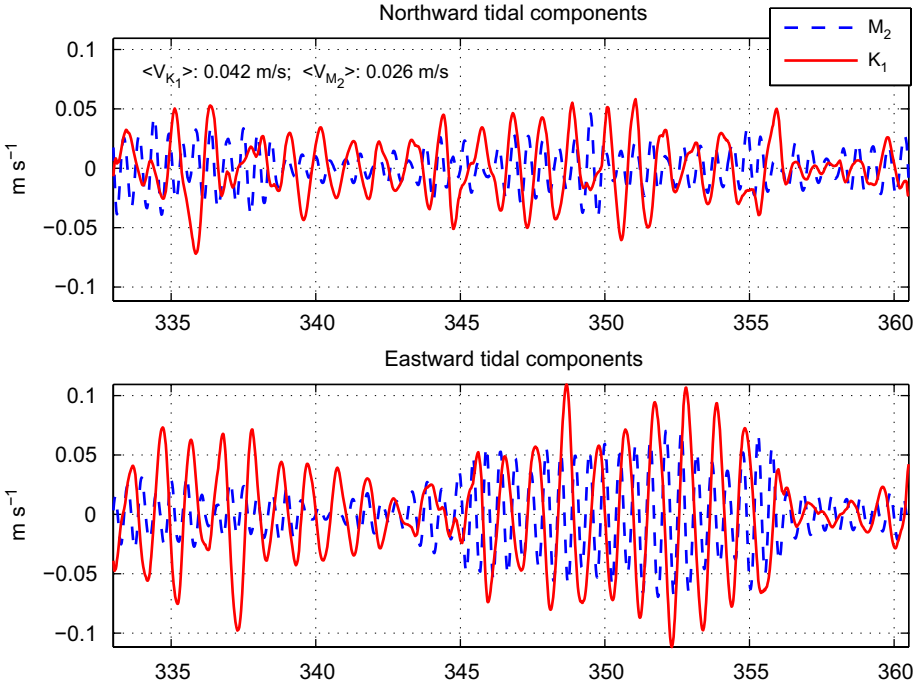

Fig. 2. Diurnal (K_1) and semidiurnal (M_2) components of ice drift for Drift 1. These are obtained by fitting complex ship GPS position vectors to complex exponential basis functions with clockwise and counterclockwise rotating components at the M_2 and K_1 tidal frequencies. Fits are calculated every 90 min, over a 1-day wide window.

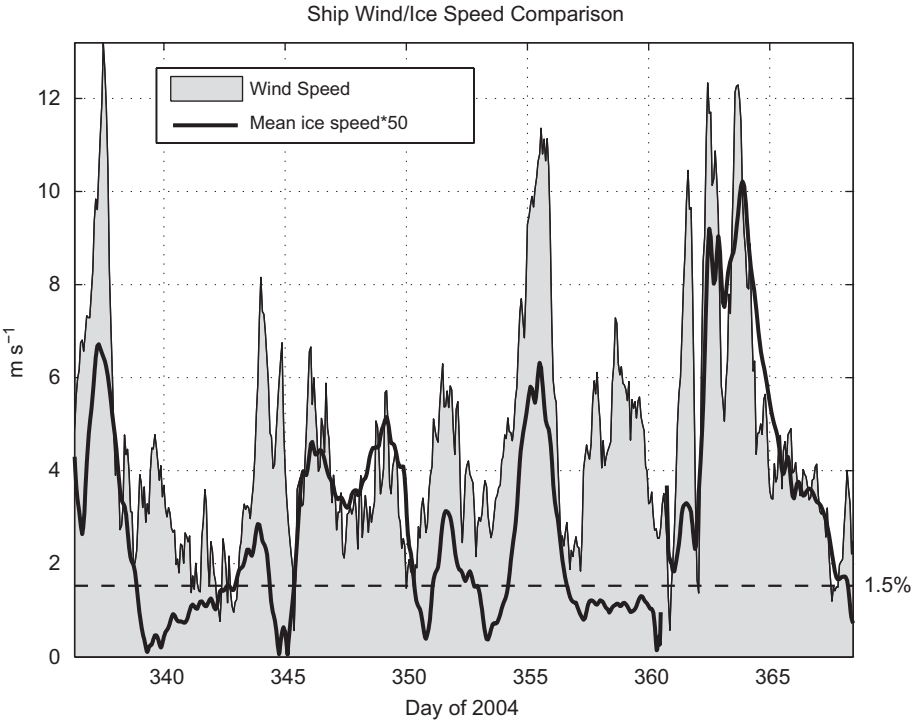

Fig. 3. Ship wind speed, averaged in 3-h blocks during the two ISPOL drift segments. Ice drift speed (after removing semidiurnal and diurnal oscillating components) multiplied by 50 is shown by the heavy black curve. The average ratio of drift speed to wind speed (adjusted to the 10-m level) is indicated by the dashed line.

corresponding times to remove the drift component. Surveys were done on 14 December (day 349), 22 December (357) and 29 December (364). The floe was constantly interacting with its surroundings; indeed, by the time of first survey on 14 December, its area had decreased markedly due to breaking-off of a large section (“Site 6”) to the southwest (see Hellmer et al., 2008). Rotation of the floe was estimated from ship heading, generally a good approximation as the moorings remained fairly taut. In the afternoon of 24 December, a sizable crack appeared off the bow of R.V. *Polarstern*, running ESE. By Christmas morning this had developed to a full-blown breakup of the main ISPOL floe, forcing rapid recovery of several science programs, including the main on-floe meteorological stations and the ocean turbulence mast. These were redeployed on the remnant of the floe on 26 December (Hellmer et al., 2008) and remained until the station was abandoned on 2 January 2005 (day 368).

3. Ocean turbulence program measurements

3.1. Deployment configurations

Table 1 summarizes five configurations in which the TIC instrumentation was deployed during ISPOL. The hydrohole at site OT-I was in 2 m of ice with snow initially about 1 m deep, and little freeboard. The first deployment comprised the main SBE 911+ system with two TICs spaced 4 m apart, and the RDI upward and downward looking ADCPs. It was suspended by cable from a winch mounted over the hydrohole. For the second deployment (OT-Ib), another TIC was suspended independently on a fixed mast, with cables to the backup SBE911+ system that remained on the surface. The Sontek 500 kHz ADP, brought along as a spare, was affixed to the bottom of the fixed mast. In the third configuration (OT-Ic), all three TICs were mounted on one mast as a unit, with the Sontek ADP on a separate mast in the same hole with the transducer head just below the ice undersurface. During the floe breakup on Christmas morning, the entire OT program was recovered and brought back aboard. With only about a week left in the drift phase, an abbreviated mast, using the backup SBE911+ was emplaced in thin ice near the snow survey line (C. Haas, personal comm., 2004) on the surviving portion of the floe. One cluster was in place by late on 26 December, with the second added by noon the next day. Final recovery of the OT program was accomplished by late afternoon on 1 January 2005.

3.2. Acoustic Doppler profiler measurements

The performance of both RDI acoustic Doppler profilers, which occupied the bottom section of the turbulence mast, was disappointing. We were unable to establish a set of parameters for the 1.2 MHz Workhorse instrument that functioned properly in the under-ice environment. Field checks of the 5-beam, broadband 0.6-MHz instrument seemed to indicate it was functioning properly; however, subsequent analysis established that noise in two of the beams needed for one horizontal

Table 1
Ocean turbulence deployment schedule

Deployment	Time	Turbulence cluster	Nom. dist. to interface (m)	Sontek ADP elevation
OT-Ia	1-December 18:00 (336.75) to 8-December 18:00 (343.75)	1:*T*, *C*, μC, *U*	4	N/A
		2:*T*, *C*, *U*	8	
OT-Ib	10-December 00:00 (345.00) to 18-December 09:00 (353.375)	1:*T*, μC, *U*	2	−8.7 m
		2:*T*, *C*, *U*	4	
		3:*T*, *C*, *U*	8	
OT-Ic	19-December 18:00 (354.75) to 25-December 06:00 (360.25)	1:*T*, μC, *U*	2	−5.5 m
		2:*T*, *C*, *U*	6	
		3:*T*, *C*, *U*	10	
OT-IIa	26-December 21:00 (361.875) to 27-December 12:00 (362.50)	1:*T*, *C*, μC, *U*	1	−6.0 m
OT-IIb	27-December 15:00 (362.625) to 1-January 05 12:00 (367.50)	1:*T*, *C*, μC, *U*	1	−8.0 m
		2:*T*, *C*, *U*	3	

component of velocity contaminated results enough to make them of questionable usefulness. Compasses and tiltmeters in each instrument did perform well and were used to establish orientation of the turbulence mast.

A backup Doppler profiler unit (Sontek 500 kHz ADP) was deployed for much of the experiment after day 345. At OT-I, when the RDI instruments were part of the turbulence mast, the Sontek ADP was deployed on its own mast. Velocities measured in the upper few bins of the Sontek ADP at the OT-I site were often suspect, in that the angular shear between 10 and 14 m was often large and ADP current direction at 12 m was very different from current direction measured with the TIC #3 ADV at 12 m. In general, the latter instrument was consistent with ADP measurements at lower levels (after accounting for some of the Ekman turning described below). This may have been because the separate turbulence mast, which extended to about 15 m depth, interfered with the doppler returns. For depths greater than 15 m, the ADP profiles were reasonably well-behaved. At OT-II, the ADP was deployed as the lower unit on the turbulence mast, so encountered no such interference.

The ADP data were averaged in 3 h bins, then sampled at fixed depths by linear interpolation. The relative (i.e. measured with respect to the drifting ice) velocities were added vectorially to the ice velocity, averaged similarly, to obtain absolute currents. Absolute current components at 20 m are compared with ice motion in Fig. 4. In the first period (345–351), the mixed diurnal/semidiurnal tidal signal was apparent in both components, but note that the shear in velocity occurred predominantly in the N-S direction. During this time the wind and ice speed were well correlated (Fig. 3). The later period (356–360) provides an interesting contrast. Here the tidal components were relatively weak and in general, the ice velocity was small: mean drift speed during the period was less than 3 cm s^{-1}. However, starting on day 359, there was a relatively strong current at 20 m setting SSW at first, but veering to mostly westward by late afternoon. In the meantime, the ice had remained almost still, despite moderate wind (Fig. 3). On day 359, the wind was also mostly westward, so for the ice to have remained still, its internal stress gradient was directed away from the shelf and was strong enough to counteract the combined forcing of wind and current. Hence, it is reasonable to conjecture that the anomalous current, combined with the wind, contributed to the Christmas breakup early on day 361.

Despite considerable vertical structure in individual ADP current profiles, there was nearly always some counterclockwise (leftward) deflection of the current (to an observer on the ice) with increasing depth. To investigate this in a "mean" sense, the 3 h average ADP data were perused for (i) profiles that were "complete" from 10 to 30 m depth (i.e. samples for which the signal to noise ratio exceeded 5), and (ii) where the velocity at 30 m was greater than or equal to 0.06 m s^{-1}. The 82 profiles meeting these criteria were then "non-dimensionalized" by forming the complex ratio $\boldsymbol{V}_n/\boldsymbol{V}_{30}$, where $\boldsymbol{V}_n$ refers to the velocity at discrete levels from 10 to 28 m depth. The resulting complex ratios were averaged and plotted as vectors (Fig. 5) to form a "spiral hodograph." Viewed from this perspective, i.e. by non-dimensionalizing with current measured near what is typically the far extent of the boundary layer, the average currents show a relatively well-behaved Ekman spiral.

3.3. Mixed-layer temperature and salinity

Except for a short period at the start of OT-II, the turbulence mast included two paired Sea-Bird T/C pairs from which salinity was calculated. A more or less continuous record of mixed-layer temperature and salinity was obtained as shown in Fig. 6. There were indications of diurnal temperature cycling during some periods, e.g., after day 355. This was most likely associated with solar elevation, since the diurnal tidal signal was relatively weak then (Fig. 4). Starting on about day 345, there was a persistent freshening trend in mixed-layer salinity. This

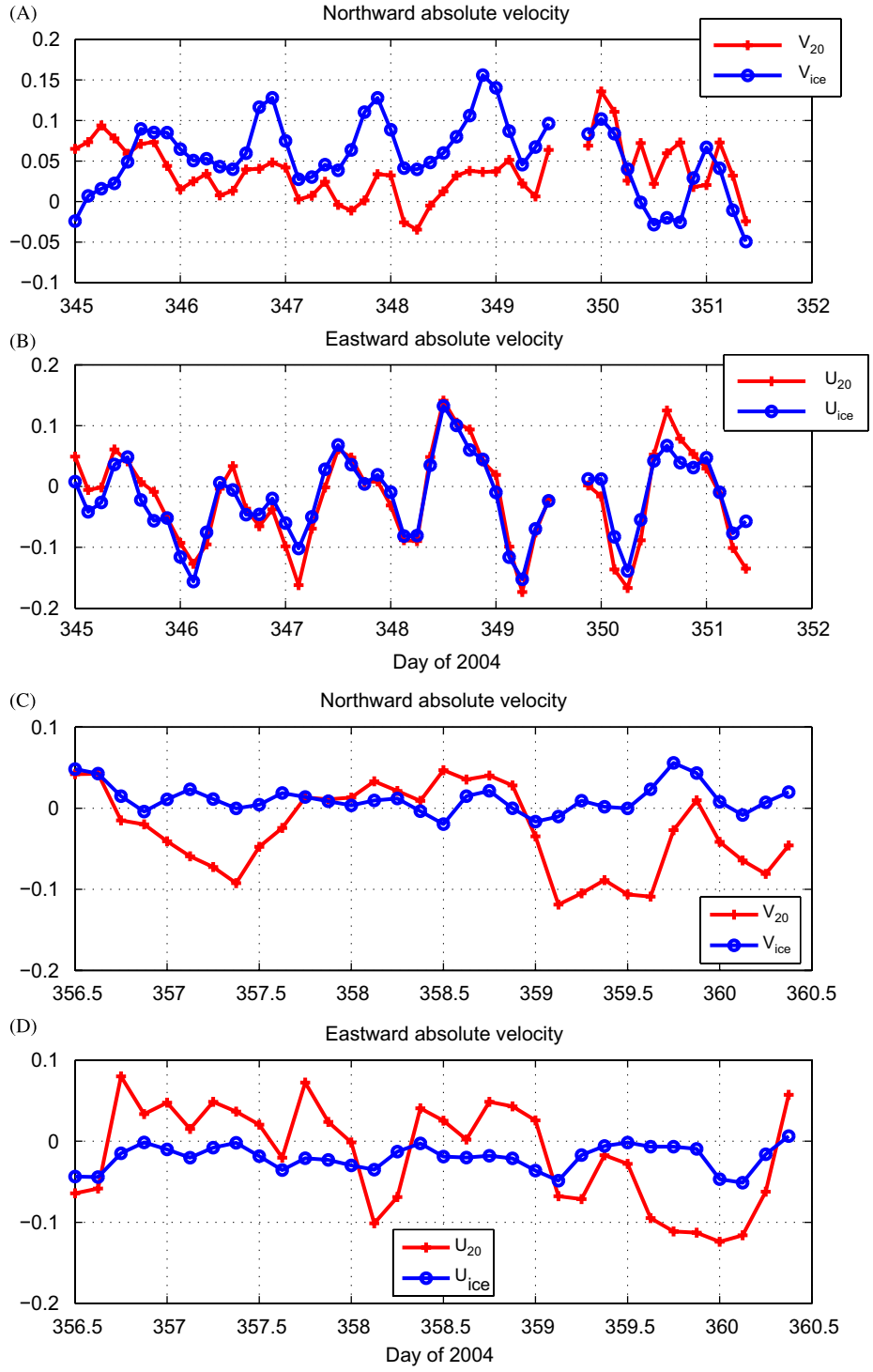

Fig. 4. Absolute currents at 20 m depth compared with ice velocity: (A) northward component, starting on day 345 (10 December), (B) eastward component, (C) northward component starting at 356.5 (noon UT on 21 December) and (D) eastward.

could result either from freshwater input associated with melting ice, or from advecting northward in an existing salinity gradient. The latter cannot be ruled out, but is inconsistent with a more or less steady increase in salinity in the water column between 100 and 200 m depth over the same time. The freshening is discussed further in Section 5.

3.4. Turbulent Reynolds stress

Turbulence statistics were assembled using techniques developed from previous projects and described in detail elsewhere (e.g., McPhee, 1992, 2002). Briefly, each 15-min segment of flow is treated as a "realization" in which, by

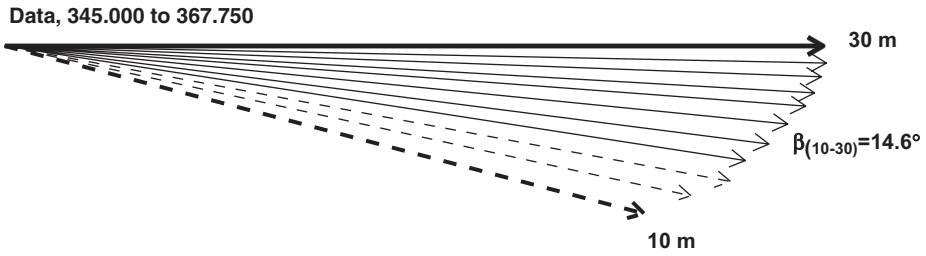

Fig. 5. Average non-dimensional current hodograph showing plan view of complex current ratios at each depth relative to 30 m, from 3-h ADP profiles as described in the text. Solid arrows represent the entire ADP record of 82 3-h averages. Dashed arrows in the upper 3 bins are for OT-II only, comprising 43 samples.

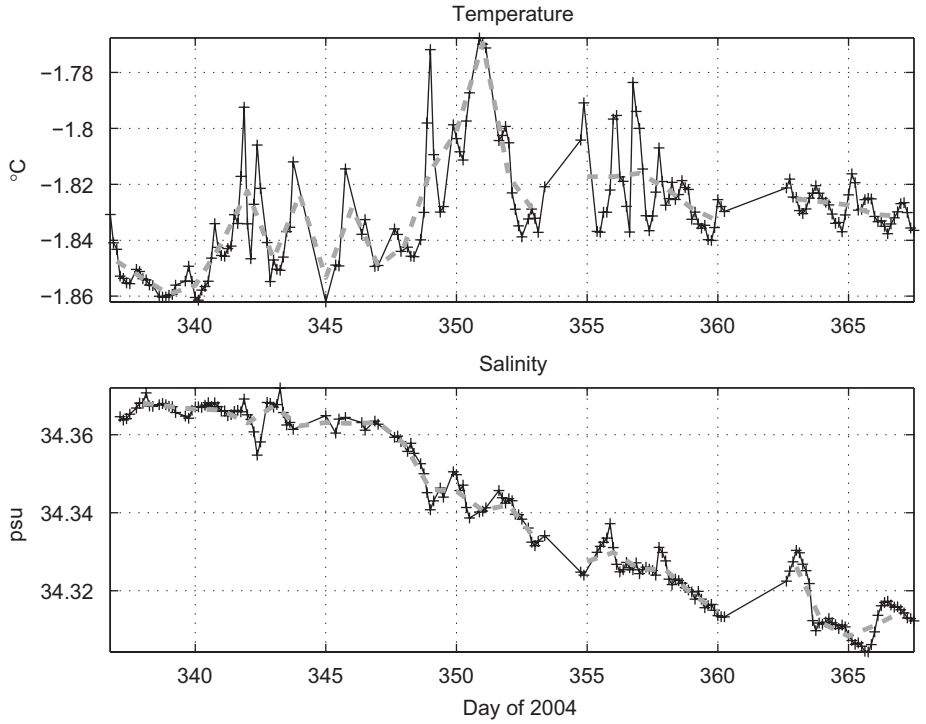

Fig. 6. Mixed-layer temperature and salinity measured via the turbulence mast. Solid curves with + symbols indicate 3-h averages. Heavy-dashed curves connect daily averages. Sensor depth varied slightly but was generally 4 or 6 m below the ice/water interface at OT-I and 3 m below at OT-II.

Reynolds analogy, the time series of deviatory velocity, temperature, and salinity (where deviatory means departure from a linear trend fitted to the actual time series) represents a "frozen-in-time" ensemble average along the mean current path. The six independent components of the Reynolds stress tensor are then estimated from the covariance matrix of the three deviatory velocity components. By common usage, the kinematic "Reynolds stress" is defined as a horizontal vector comprising the covariance of vertical velocity with the two horizontal components, i.e. in complex notation $\boldsymbol{\tau} = \langle u'w' \rangle + i\langle v'w' \rangle$, with velocity-squared units. For convenience, we define a turbulence scale velocity called friction velocity, which is a vector in the same direction as the Reynolds stress with magnitude equal to its square root. Friction speed, $u_* = |\boldsymbol{\tau}|^{1/2}$, refers here to the *local* turbulent scale speed, as opposed to its value at the interface, henceforth referred to as u_{*0}.

The 15-min turbulence averaging interval is chosen to fall in a "spectral gap," capturing the covariance in the turbulence motion, but avoiding contamination from longer-period variability. The "energy containing" eddies in under-ice turbulence often persist for up to 1–2 min, hence there is a large variability from realization to realization, even in a relatively steady flow. For this reason, covariances calculated from the 15-min realizations were further averaged in 3-h time bins to reduce this natural variability, and to assign all the measurements to a common time base. Friction velocity for the separate deployment schemes (except OT-IIa, which was short) are shown in Fig. 7. The values for the most part agree reasonably well; however, it is clear for the cluster nearest the ice/water interface (1 or 2 m), the friction speed is nearly always smaller than at deeper levels, in contrast to expected behavior if the ice undersurface were horizontally homogeneous.

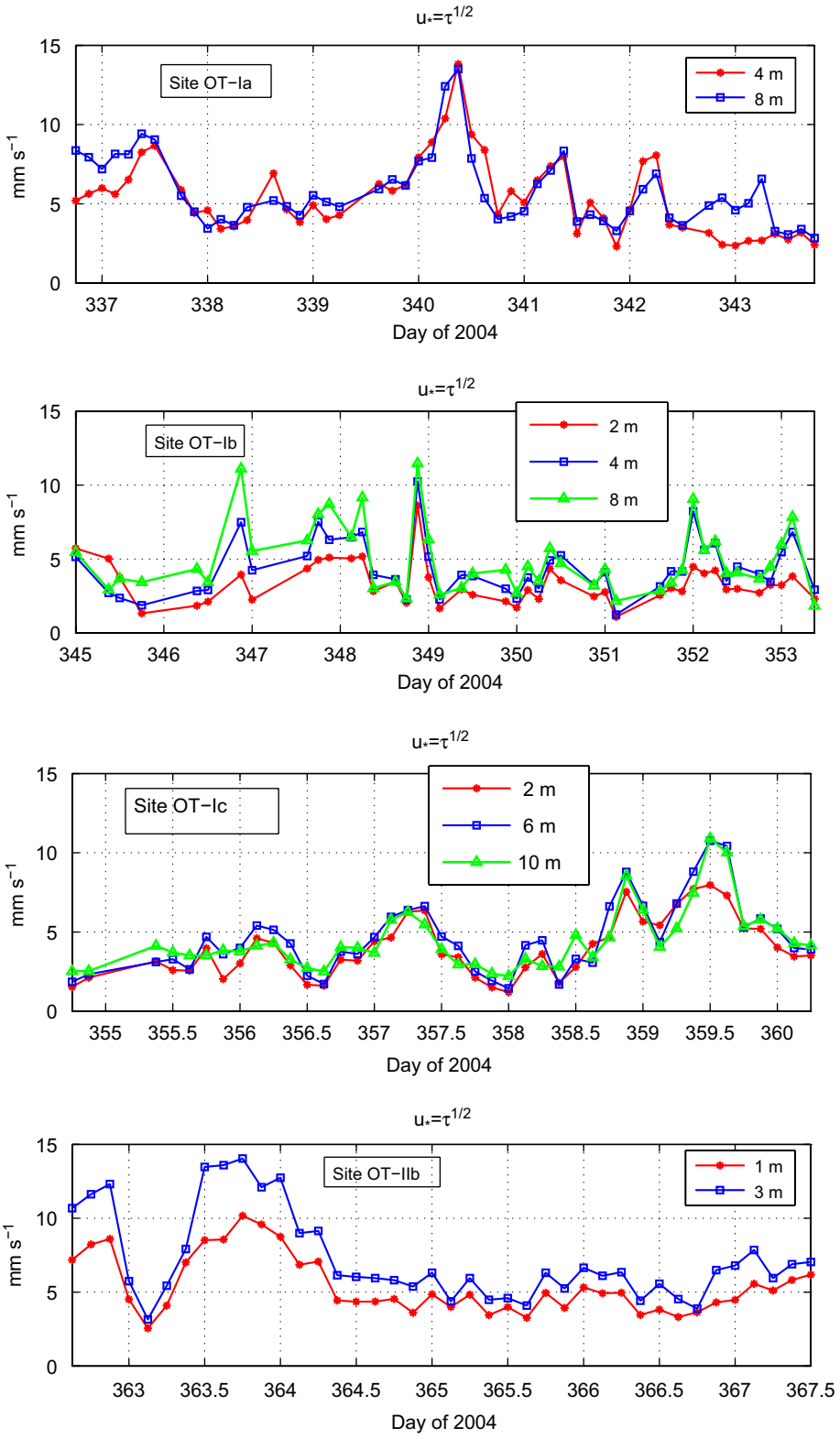

Fig. 7. Friction speed (square root of local kinematic Reynolds stress) for the main turbulence mast configurations listed in Table 1.

3.5. *Turbulent heat flux*

Turbulent heat flux was calculated from the covariance of deviatory temperature and vertical velocity, multiplied by the product of density, ρ, and specific heat for seawater, c_p. Time series during the various mast configurations (Fig. 8) illustrate large variation with periods of downward heat flux at all levels (e.g., 356.875); mixed upward and

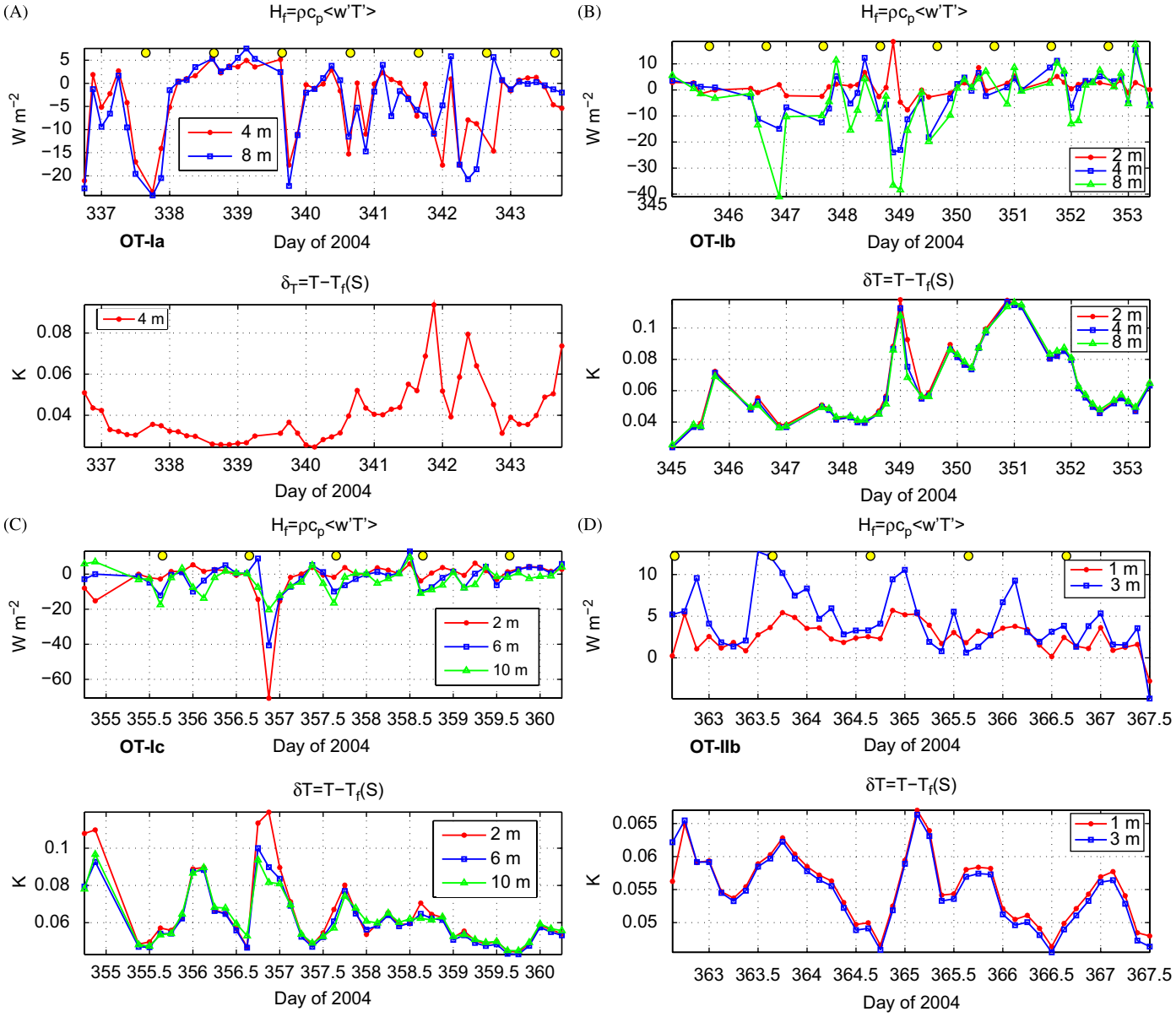

Fig. 8. Turbulent heat flux time series for the mast configurations listed in Table 1 (upper panel), plus the elevation of seawater temperature above freezing (δT, lower panel). Yellow symbols at the top of each heat flux plot indicate local noon at longitude 55°W. For TIC 1, δT was determined by assuming mean salinity to be the same as TIC 2.

downward at other times (e.g., 348.875); and small upward flux at all levels (358.5 and all of OT-IIb except the last sample). Generally, when sea ice floats in above freezing water, we expect upward flux at the interface, and previous measurements have shown consistently that the heat flux is nearly proportional to the product $u_*\delta T$ where δT is the elevation of mixed-layer temperature above freezing (McPhee, 1992; McPhee et al., 1999). At OT-II, this relationship appears to hold, at least qualitatively, but for OT-I any correlation is tenuous at best, even 2 m below the interface.

The proximity of OT-I to the floe edge undoubtedly affected heat flux measured in the water column there. The largest measured downward heat flux ($-71\,\mathrm{W\,m^{-2}}$, 2 m below the ice) occurred at time 356.875, and coincided with relative current emanating almost directly from the open lead about 70 m away (Fig. 9). It coincided with maximum observed δT, as well as having a large temperature gradient between the upper and lower cluster (Fig. 8C). An earlier time (348.875) provides an interesting contrast (Fig. 10). At the same time of day, heat flux measured at the lower two clusters is roughly the same as in Fig. 9, but at the 2 m level, heat flux is about $20\,\mathrm{W\,m^{-2}}$ upward. In this case the ice is moving much faster, and the friction velocity at 2 m is more than double the later value. The main difference, however, is that relative flow approaches across a much longer fetch across an old pressure ridge between the R.V. *Polarstern* and the OT-I site. A reasonable interpretation is that here

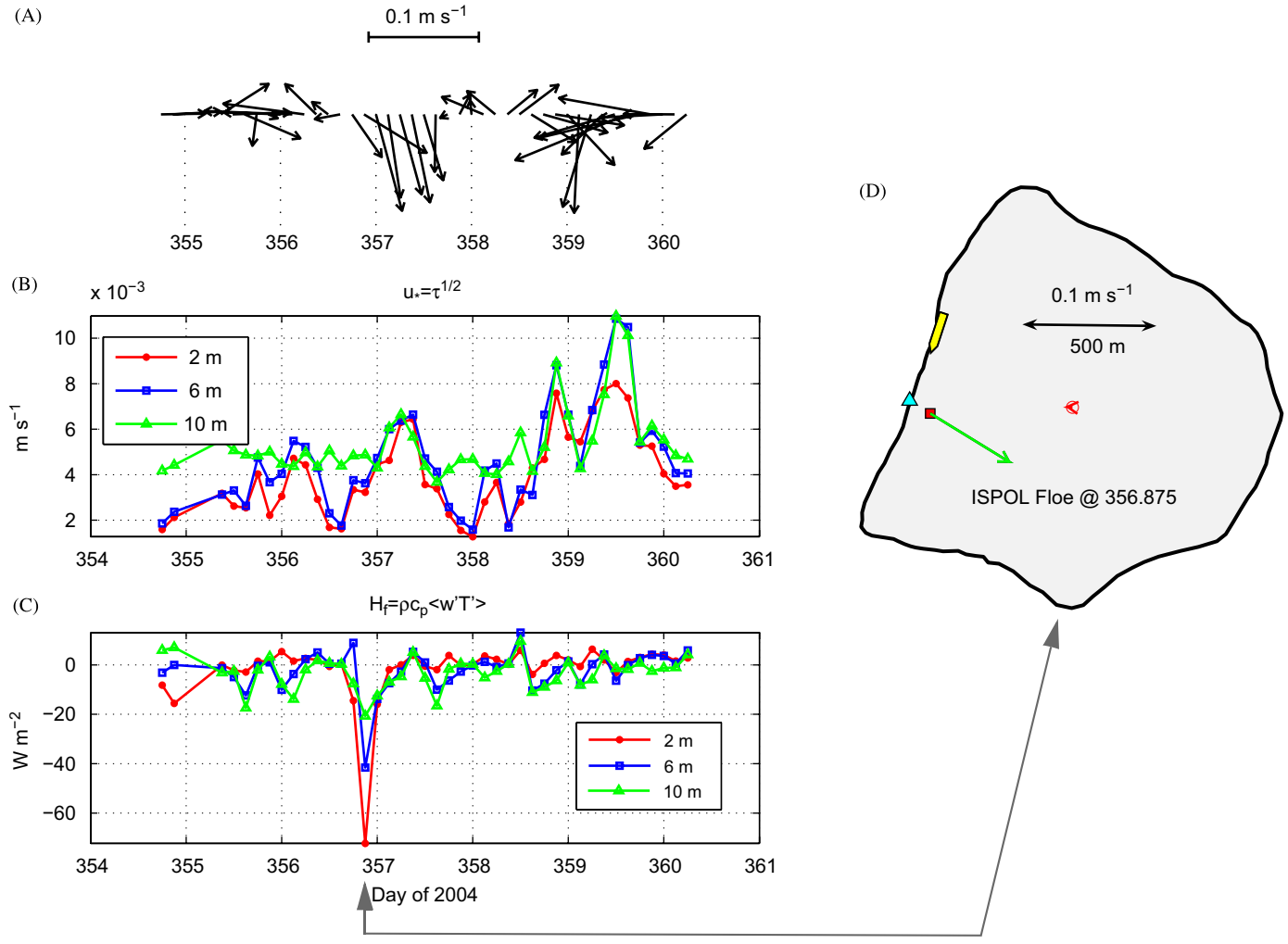

Fig. 9. (A) Current vectors as measured at 2 m during OT-Ic. North is up. (B) Turbulent friction velocity at listed distance from the ice/water interface. (C) Turbulent heat flux. (D) Floe outline showing the OT-I position (red square) with respect to R.V. *Polarstern* (yellow polygon) and floe edge opposite current direction (triangle) at time of maximum downward heat flux. Ice velocity indicated by the red arrow at the center is almost zero.

the lower clusters are "seeing" the effect of upstream solar heating in the lead to the stern of the ship and beyond, while the 2-m cluster is within an internal boundary layer adjusting to more local conditions. While δT is roughly the same as for the later example, the temperature difference between TICs 1 and 2 is small. The upward heat flux at 2-m thus represents extraction of heat from the mixed layer, associated with ice melting at the interface, while the negative flux lower is downward mixing of absorbed solar energy.

The large variability in flow directions (hence fetch across unbroken ice; at $0.1\,\mathrm{m\,s^{-1}}$, the scale vector in Fig. 10D is traversed in about 83 min), combined with large vertical variability in measured heat flux, accentuates the difficulty of extrapolating heat flux measurements directly to interface conditions.

3.6. *Turbulent salinity flux*

Two types of conductivity sensors were utilized in the ISPOL turbulence program: the standard, ducted SBE04 conductivity meters, and the open-electrode, SBE07 μC sensor. Each had drawbacks. The standard cells are ducted to retain long-term accuracy, but this limits their ability to track rapid changes as turbulent eddies sweep past the sensors. This imposes a high wavenumber cutoff that potentially limits their capacity to capture the actual w, S' covariance. In comparing data from a standard cell with a μC instrument in forced-convective conditions at the edge of a freezing lead, McPhee and Stanton (1996) showed that the covariance in salinity calculated from the standard cell was about 70% of the value from the μC instrument. Since the length scale and period of the largest eddies in the statically unstable stratification was significantly larger than for neutral conditions, this probably represents an upper limit.

The open-electrode microstructure probes respond rapidly to changes, but are prone to significant calibration drift, and to biofouling. Our experience with the μC probes during ISPOL was mixed. Although there were times when they tracked longer-period changes observed in the standard cells reasonably well, much of the time the

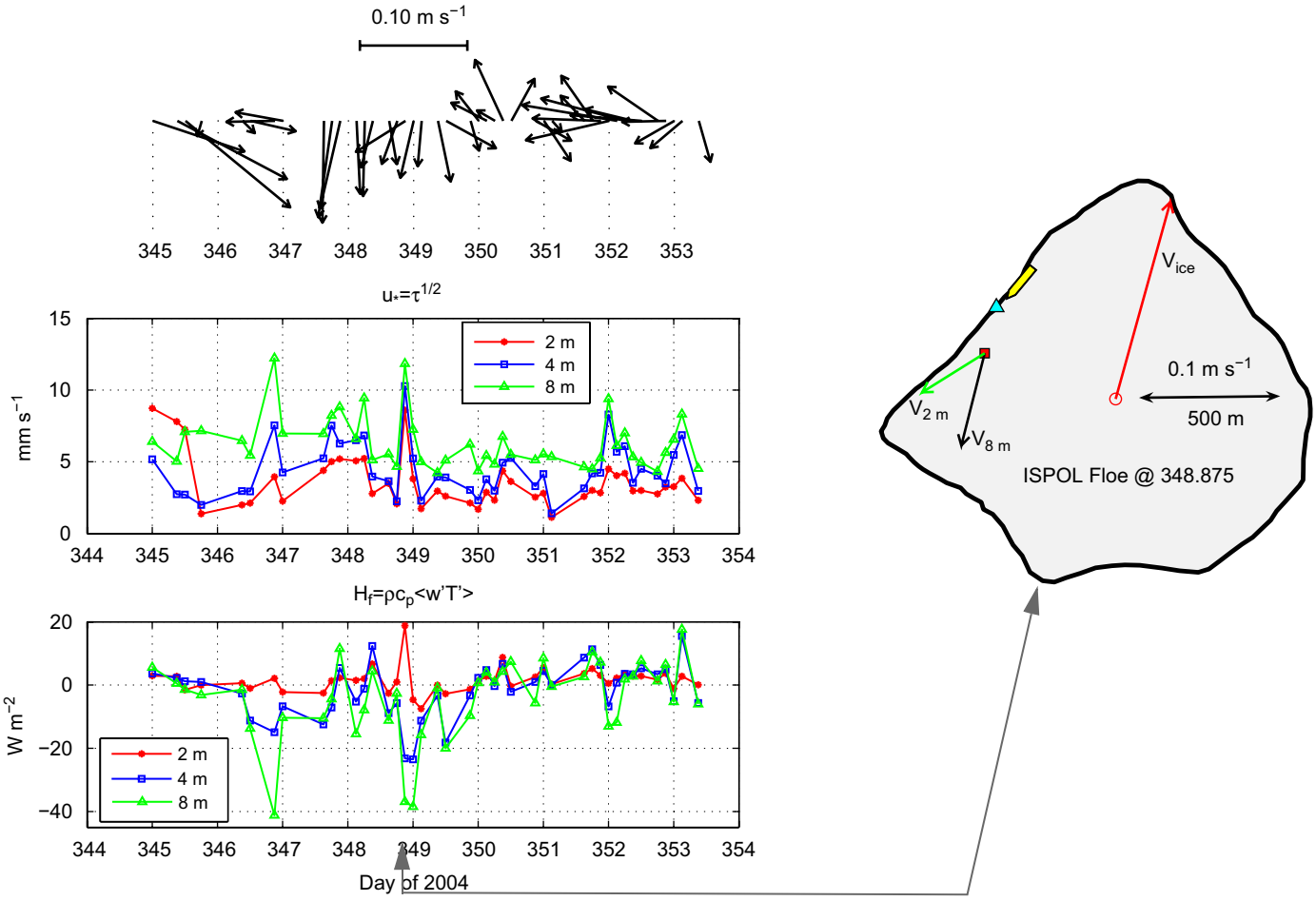

Fig. 10. Same as Fig. 9, except earlier time during OT-Ib with larger stress and different flow direction, indicated by the 2- and 8-m vectors in (D). Vector labeled V_{ice} is the 3-h average ice velocity.

variance in the μC data was unrealistically large. This may have resulted from biofouling, or damage to the delicate electrodes during handling. We choose not to present those results until more advanced analysis shows when the μC fluxes were valid.

S', w covariance based on the standard C cells is shown in Fig. 11. For the most part, the values at TICs 2 (4–6 m) and 3 (8–10 m) during OT-I (b, c) are well correlated. Mean values for OT-I are 5.3×10^{-7} and 9.8×10^{-7} psu m s^{-1}, for clusters 2 and 3, respectively. For OT-II after the station relocation, the salinity flux is predominantly downward, with mean values of -9.6×10^{-7} and -12.3×10^{-7} psu m s^{-1}, for clusters at 1 and 3 from the ice, respectively.

4. Analysis

4.1. Mixing length

Simple dimensional analysis arguments suggest that relating vertical turbulent flux of a property in the boundary layer to its mean gradient requires a factor that depends on the product of a turbulent scale velocity and a length scale over which eddies are effective at diffusing the particular property. If the scale velocity is u_*, the *eddy viscosity* may be written $K_m = u_*\lambda$, where λ is the *mixing length*. In the neutrally stratified atmospheric surface layer, λ is simply $\kappa|z|$ where κ is Karman's constant, 0.4, and expressing $K_m = \kappa u_*|z|$ leads directly to the "law-of-the-wall" (LOW)

$$\frac{U(z)}{u_*} = \frac{1}{\kappa}\log\frac{|z|}{z_0} \quad (1)$$

where U is current speed at level z.

Our previous measurements in the under-ice boundary layer (e.g., McPhee, 1994, 2002) indicate that the scale of turbulence in natural shear flows is controlled mainly by the smallest of the three scales: $\kappa|z|$, κL, or $\Lambda_* u_*/f$ where L is the Obukhov length (inversely proportional to the buoyancy flux), and Λ_* is a similarity constant. McPhee and Martinson (1994) suggested a value of 0.028 for Λ_*. Thus an idealized mixing length when buoyancy is negligible can be represented as linear in u_*/f until it reaches a limiting value determined by $\kappa|z|$.

We have also found in previous work (McPhee and Martinson, 1994; McPhee, 1994, 2004) that the inverse of the wavenumber at the peak in the area-preserving

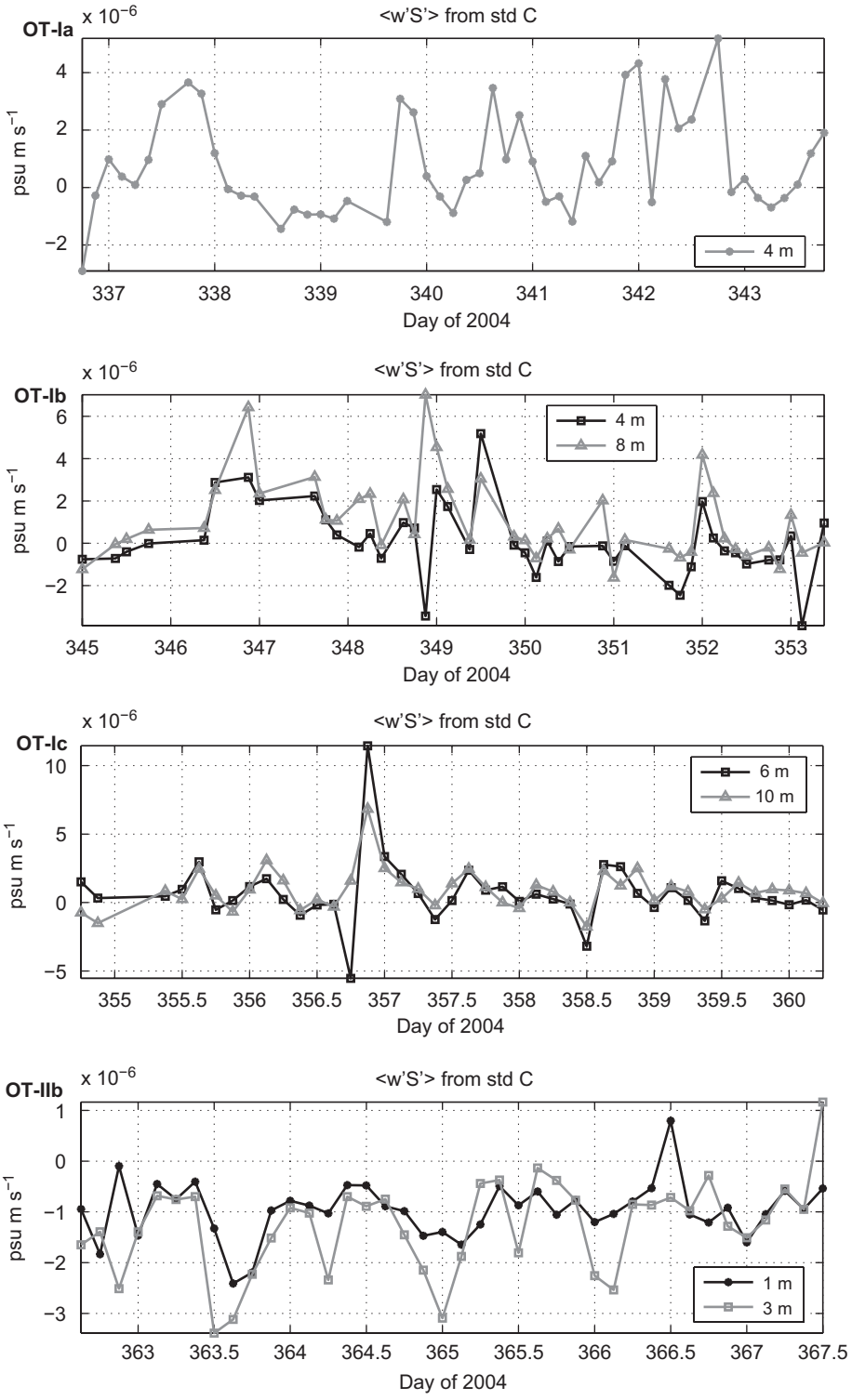

Fig. 11. Three-hour average salinity flux estimates from salinity evaluated with the standard SBE04 conductivity cells. Distance from the ice/water interface is indicated. A bad cable connection eliminated conductivity data for TIC 2 at 8 m during OT-Ia.

(weighted) variance spectrum of vertical velocity provides a good proxy for the mixing length, even in those regions where the LOW is no longer valid. An example from a typical 3 h average of spectra calculated from 15 min realizations from Site OT-II (Fig. 12) illustrates the method, which in this case yields an abscissa value of -0.82, or $\lambda = 1.0$ m, with $c_\lambda = 0.85$.

A distribution of λ calculated as above for each 3-h average from all turbulence clusters at Site OT-I plotted against the covariance estimate of u_* is shown in Fig. 13.

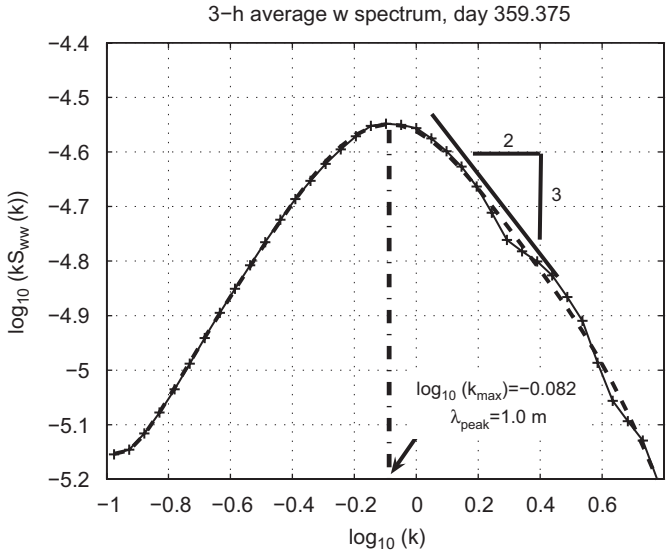

Fig. 12. Area-preserving, average w spectrum for 3 h centered at 0900 UT, 24 December 04. The average is formed by calculating spectra for each 15-min realization, with frequency converted to wavenumber by Reynolds analogy using the mean current speed. Spectral estimates are then averaged in fixed wavenumber bins, and fitted with a high-order polynomial (dashed curve), from which the maximum (dot-dashed line) is determined.

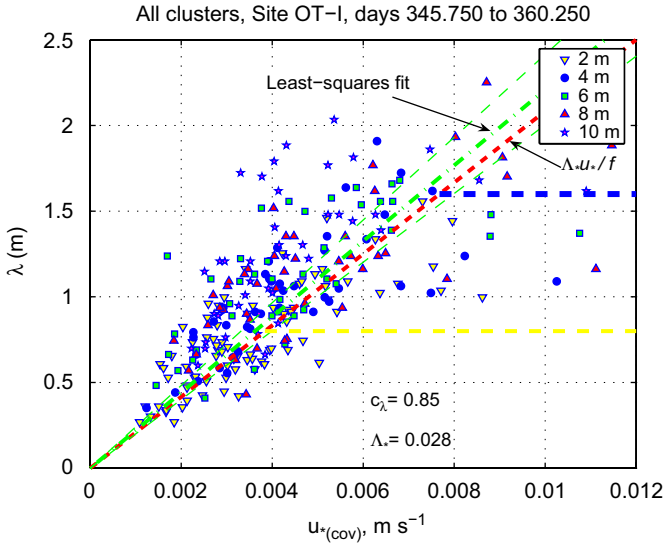

Fig. 13. Scatter plot of mixing length λ versus u_* for all 3-h averages during deployment OT-I. The dashed (red) line is the "planetary limit:" $\Lambda_* u_*/f$. The horizontal dashed lines represent the "geometric limit:" $\kappa u_* |z|$, at 2 m (yellow) and 4 m (blue), respectively. The dot-dashed line with 95% error limits (thin dashed) is a least-squares fit through the origin.

This was the first relatively long deployment in a multiyear under-ice environment of the backscatter acoustic current meters. By sampling an undisturbed flow volume with no mechanical constraints, they provided measurement of significantly lower levels of stress than were available previously. Results indicate that λ follows the "planetary scale" ($\Lambda_* u_*/f$) rather than the geometric scale ($\kappa u_* |z|$), even relatively close to the interface.

4.2. Undersurface roughness

While it is common to express the flux of momentum (stress) between sea ice and the underlying ocean in terms of a drag coefficient, it is often advantageous to express the frictional parameter as a "roughness length," z_0, because it (i) obviates the need for restricting the drag formulation to currents at a particular depth, and (ii) leads naturally to a Rossby-similarity expression for stress in terms of the ice velocity relative to the underlying geostrophic current in the ocean. The latter does not in fact follow a strictly quadratic stress rule.

It is relatively easy to relate turbulent stress and mean velocity (measured relative to the ice) in a neutrally buoyant boundary layer via (1), provided (i) the undersurface is horizontally homogeneous; (ii) measurements are made within the surface layer (i.e. where mixing length is governed by the geometric scale κz); and (iii) the geometric scale is less than the limiting planetary scale $\Lambda u_*/f$. Conditions at both ISPOL sites consistently violated one or all of these conditions (which indeed are difficult to satisfy under pack ice anywhere), hence determination of the undersurface roughness and a representative parameterization of ice/ocean stress are less than straightforward.

4.2.1. Direct estimates of z_0

As with other studies under multiyear pack ice (McPhee, 2002), Reynolds stress at ISPOL often increased with increasing distance from the interface (Fig. 7), reflecting the heterogeneous nature of the ice underside. As depth increases, turbulence is affected by roughness elements increasingly farther upstream (for practical reasons, instrumentation is usually deployed under relatively smooth ice). The upstream distance affecting turbulence some distance from the interface may be estimated roughly by the ratio U/u_*, where U is the horizontal current speed (Morison and McPhee, 2001). For pack ice, a representative ratio is 15, hence measurements 2 m from the ice might sense roughness elements within say, 30 m, whereas turbulence 4 m lower would be affected by roughness elements as much as 100 m away. If ice is relatively smooth within the former horizontal distance but includes keels and hummocks within the latter, one would expect measurements at the upper level to indicate a smoother surface (smaller z_0) than the lower measurements. Site OT-I was near the center of a trapezoidal section of 2-m-thick ice bounded on three sides by modest pressure ridges (ranging in minimum distance from roughly 40 to 60 m), and on the fourth by the lead in which R.V. *Polarstern* was moored (Hellmer et al., 2008, their Fig. 2). Within 20–30 m of the mast, underwater video confirmed that the ice underside was very smooth (R. Kiko, personal comm., 2004).

At Site OT-II, located in thinner (1-m) ice, the surroundings were more complex. There was a modest pressure ridge relatively close to the installation on one

side, and smooth ice toward the floe edge on the other. The ridge was initially situated to the west, but after a nearly 90° counterclockwise rotation on day 362, it was north of the turbulence mast, and at times had profound influence on turbulence and shear in the upper ocean, as indicated by the marked decrease in U/u_* when flow approached from across the ridge (Fig. 14). As it turned out, the relative flow was quite often from the NE, so turbulence was advected from upstream to the OT-II site more energetically than at OT-I, with large impact on the turbulence parameters.

We used two methods to relate local measurement at the uppermost two instrument clusters to z_0. The first is direct application of the LOW, (1), using 3-h averages of U/u_*. The second is called the mixing-length-method (MLM) as adapted directly from McPhee (2002), to which the reader is referred for mathematical details. In addition to U and u_*, it considers λ_m as determined from the w spectra in Section 4.1, plus a minor correction to friction velocity $u_{*_0} = u_*\left[1 - \left|z_m/(2h_{ml})\right|\right]$ associated with the extent of the well-mixed layer, h_{ml}. In this approach, if $\lambda_m > \kappa|z|$ at the measurement level, turbulence is more efficient at transporting momentum, hence the momentum flux can be accomplished with a smaller surface roughness than would be computed from the LOW. The drag law is then

$$\log z_0 = \log|z_m| - \frac{|z_m|}{2h_{ml}} - \frac{\lambda_m U}{|z_m| u_{*_0}} \qquad (\lambda_m \geqslant \kappa|z_m|) \tag{2}$$

Conversely, if the $\lambda_m < \kappa|z|$, the method assumes that the turbulence is constrained by a dynamic scale rather than geometric, thus the boundary layer between the surface and the measurement levels comprises both a wall layer and an "outer" layer where the mixing length is assumed constant. In this case turbulence is less efficient than for the LOW, and the surface roughness would be correspondingly larger than that implied by the LOW. The drag relation is thus

$$\log z_0 = \log\frac{\lambda_m}{\kappa} - \frac{\lambda_m}{2\kappa h_{ml}} - \frac{\kappa U_{sl}}{u_{*_0}} \qquad (\lambda_m < \kappa|z_m|) \tag{3}$$

where

$$U_{sl} = U_m - \lambda_m u_{*_0}\left(|z_m| - \frac{\lambda_m}{\kappa}\right)\left(1 - \frac{1}{2h_{ml}}\right)$$

$$U_m = \frac{u_{*_0}|z_m|}{\lambda_m}\int_{z_0}^{|z_m|}\left(\frac{1}{|z|} - 1\right)dz$$

$$\lambda_m = \begin{cases} \kappa|z| & |z| \leqslant \lambda_m/\kappa \\ \lambda_m & \lambda_m/\kappa < |z| \leqslant |z_m| \end{cases}$$

The natural logarithm of z_0 (the basic integration constant in both the LOW and MLM) was calculated for each 3-h-turbulence sample for the upper two clusters during the entire project, using both methods. For MLM, h_{ml} was estimated by linear interpolation of the twice daily CTD stations. Results were then grouped according to distance from the interface, and the median calculated for each group at each site as shown schematically in Fig. 15. Where error bars overlap, the sample medians are not

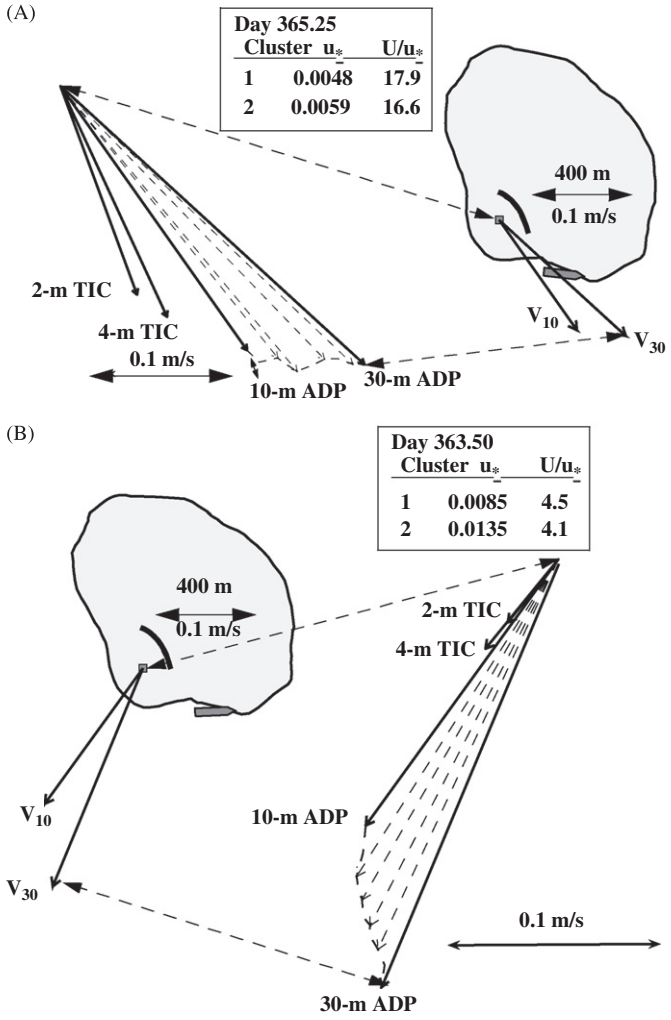

Fig. 14. (A) Three hour average currents measured relative to the drifting floe, centered at time 365.25. The shaded area represents the OT-II (Drift 2) floe (R.V. *Polarstern* is indicated by the polygon at the south end), with the location of the turbulence mast indicated by the square, and ADP currents at two levels shown as labeled vectors. The relative flow approaches from across relatively smooth ice to the NW. The heavy curve near the mast site represents a nearby pressure ridge. The vector diagram to the left shows the current structure in more detail, including the TIC levels and intermediate ADP levels. The inset box lists measured friction velocity and the ratio of mean current speed to u_*. (B) Similar to A except that a stronger relative flow approaches from the NNE across the pressure ridge keel. Note the much reduced currents near the surface, almost double friction velocity (quadruple stress), and much smaller U/u_* ratio indicating greater roughness.

statistically distinguishable with 95% confidence. Thus, unlike the SHEBA results (McPhee, 2002), the only significant difference between the two approaches occurs at OT-II, 1 m below the interface, in which case z_0 inferred from the mixing length method is more than an order of magnitude smaller than that calculated from the LOW (although confidence limits overlap slightly). Expanding from the discussion above, the upstream turbulence generated by the pressure ridge keel tends to increase λ_m relative to the geometric scale, thus, the momentum flux can be accomplished via a relatively smoother surface. The

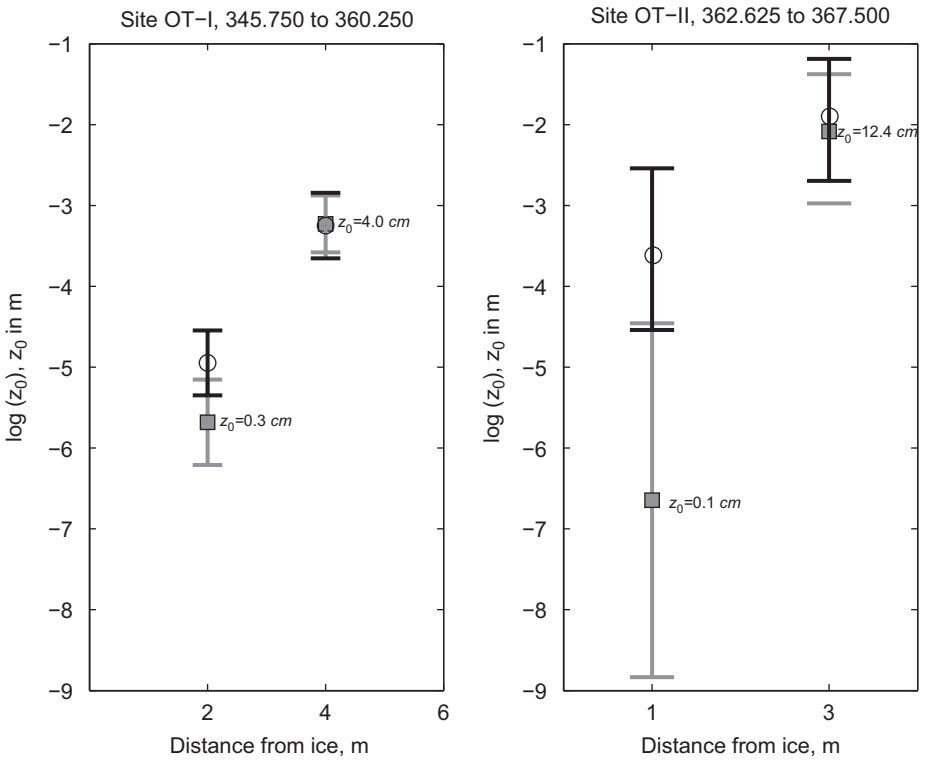

Fig. 15. Site OT-I. Median values for the natural log of z_0 determined from mean velocity and turbulent stress measured at the upper two turbulence clusters levels. Squares (gray) are from the mixing length method (McPhee, 2002); circles are direct application of the law of the wall. Error bars represent a 95% confidence interval for the median based on quartile limits. Site OT-II: same except cluster levels 1 and 3 m below the ice. The large value at OT-II, cluster 2, results from intense turbulence generated from the upstream pressure ridge keel.

effect is slight at OT-I, but pronounced at OT-II, because the flow was often there across the nearby keel. The fact that z_0 is of order millimeter scale at the upper clusters at both sites probably reflects the relatively smooth surface very near to the mast locations. At the deeper levels (4 and 3 m below the ice), the inferred roughness is considerably larger, as the upstream impact of rougher undersurface features is manifested. The roughness inferred for 3 m at OT-II is quite large, comparable to estimates in the marginal ice zone and rough multiyear pack ice. However, as indicated by the vastly different U/u_* ratios apparent in Fig. 14, this reflects the upstream impact of the pressure ridge keel, and is probably not typical of the entire floe.

4.2.2. *Indirect estimate of z_0*

Given that our estimates of z_0 from point measurements at various levels in two locations under the ISPOL floe differ by almost two orders of magnitude, is it possible to make a reasonable estimate of the undersurface roughness representative of the entire floe? How to "scale up" measurements made in one (usually fairly smooth) location under a floe has been and remains a vexing problem in understanding the exchange of momentum between sea ice and the underlying ocean. The non-dimensional treatment of the ADP data showing a well-behaved spiral structure (Fig. 5) suggests a possible approach, reasoning as follows. In general, similarity arguments (e.g., Rossby, 1932; McPhee, 1981) suggest that boundary layers in a neutrally stable atmosphere or ocean should be similar if scaled properly, except for the following. In the surface layer (i.e. where mixing length depends on distance from the surface) the total shear is highly dependent on z_0, which is a physical scale so that its non-dimensional representation, say $\zeta = fz_0/u_{*_0}$ is not fixed in a similarity sense. Consequently, if z_0 is small, shear in the surface layer is large, and the angle of turning is reduced. Suppose, we model the under-ice boundary layer over the whole range of conditions encountered during ISPOL, with results scaled by forming complex ratios of the modeled velocity with the modeled current at 30 m, and that this is executed for a number of different z_0 values. We further suppose that below some depth, the boundary layer structure reflects the overall roughness of the entire floe. Then by matching modeled turning with observed, we may be able to prescribe a reasonable value for z_0 representative of the entire floe and surrounding ice. In effect, the approach is an enhancement of the "momentum defect method," in which the integral of velocity perpendicular to stress provides a measure of the turbulent stress.

The procedure was carried out by applying the "steady local turbulence closure model" (McPhee, 1999, 2002; McPhee et al., 1999) to each 3 h average velocity profile, for a range of z_0 values between the limits implied by Fig. 15. The model does not assume neutral stability throughout, but instead combines the interpolated (in time) temperature/salinity profiles in the upper ocean as measured by the

shipboard CTD systems (data courtesy of M. Schröder), with point measurements from the turbulence clusters. The model then iterates to a solution in which the eddy viscosity adjusts to the local stress and buoyancy flux conditions. For this exercise, the model was driven by the observed relative velocity at 20 m depth, which involves an outer iteration loop. To initialize the outer loop, $\boldsymbol{u}_{*0}$ (a vector) is calculated from Rossby similarity, and the model solution (from the inner loop) for the relative current at 20 m is compared with observed. If they differ by more than some specified tolerance, the friction velocity is adjusted by the complex ratio $\boldsymbol{U}_{20(\mathrm{obs})}/\boldsymbol{U}_{20(\mathrm{mod})}$, the inner loop is repeated, and so on, until the modeled 20 m current agrees with observed.

Results are illustrated for the OT-II measurements in Fig. 16. Each 3 h average ADP profile was considered separately, with upper-ocean temperature/salinity structure interpolated from adjacent ship CTD profiles, and model velocity matched to observed velocity at 20 m. For each of three values for z_0 encompassing limits inferred from the TIC flux measurements (0.001, 0.04, 0.12 m), the model was run for all 43 samples, then modeled velocities from 10 to 30 m were non-dimensionalized by the 30 m value, and the resulting average ratios plotted as hodographs to compare with the observations. In this case, it appears that the undersurface roughness of about 0.04 m matches the turning between 10 and 30 m fairly well. This agrees well with results from the TIC 2 at OT-I (Fig. 15), and with other estimates from multiyear pack ice (McPhee, 1990).

As described above, velocities measured in the upper few bins of the Sontek ADP at the OT-I were questionable, so a second series of calculations there considered only shear between 14 and 30 m. In this case, the average observed turning between 14 and 30 m from 39 3-h average profiles was 9.1°, while modeled turning with $z_0 = 0.04$ m was 9.2°, i.e. consistent with the results for OT-II.

4.3. Heat transfer coefficient

We have found from previous drift experiments that for low to moderate ocean-to-ice heat transfer rates, the basal turbulent heat flux, H_f, is well described by the relation

$$H_\mathrm{f} = \rho c_p \langle w'T' \rangle_0 = \rho c_p c_\mathrm{h} u_{*0} \delta T \quad (4)$$

where c_h is the bulk heat transfer factor. We typically find it to be between 0.005 and 0.006, with the best estimate from the year-long SHEBA program being 0.0057 ± 0.004 (McPhee et al., 2003).

Because large vertical gradients in turbulent heat flux often were observed during the ISPOL drift (Section 3.4), estimating the ocean-to-ice heat transfer is problematic. Even though the mixed layer was consistently above freezing, indicating that heat was available for basal melting, our observations often showed negative heat flux

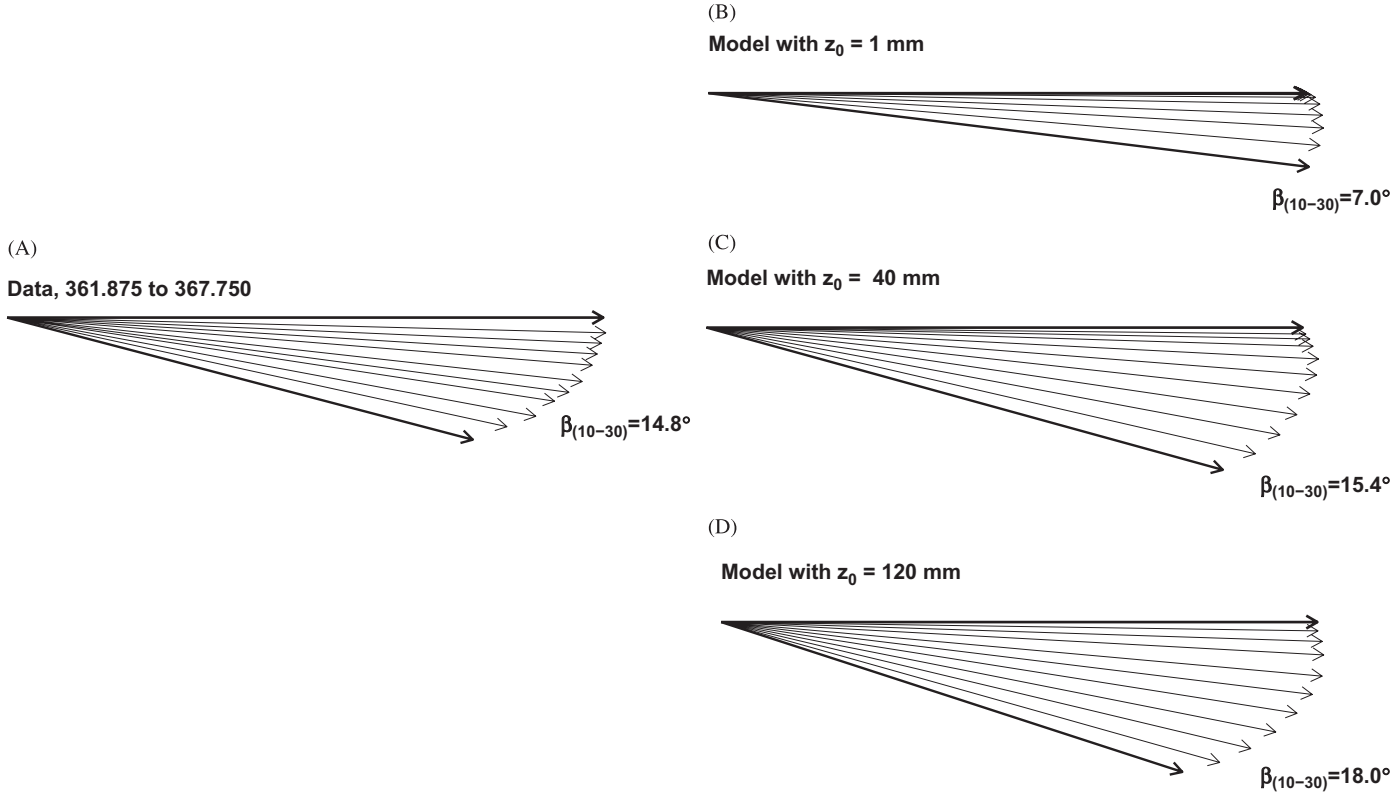

Fig. 16. (A) Average of all complex ratios calculated by dividing the complex velocity every 2 m from 10 to 28 m depth, by the complex velocity at 30 m, at site OT-II. There were 43 3 h average profiles considered for which the current speed at 30 m exceeded 0.06 m s^{-1}. β indicate the total Ekman turning between 10 and 30 m. Each profile was modeled using local turbulence closure, interpolated T/S structure, driven by the observed velocity at 20 m, for three different values of z_0. Average ratios for $z_0 = 0.001$, 0.04, 0.12 m are shown in (B–D), respectively.

in the water column, as would be expected from downward mixing of solar energy absorbed near the surface in nearby leads or under thin ice. This was apparently dependent on both the solar angle and the relative current fetch across the floe. The strength of local turbulent mixing was also dependent on distance from nearby under-ice features, particularly at OT-II.

We identified 16 3-h samples when measured heat flux at the uppermost level at OT-I exceeded $4\,W\,m^{-2}$. A regression of $\langle w'T' \rangle$ against $u_*\delta T$ resulted in $c_h = 0.0059 \pm 0.0016$ with a 95% confidence limits for a linear fit through the origin. At OT-II, heat flux was consistently upward, but there was often a significant gradient in $\langle w'T' \rangle$ between 1 and 3 m below the interface. Including the uppermost (1-m) cluster there resulted in a somewhat lower c_h value, but wider confidence limits. Thus the scatter in the data, and the overall low level of observed upward heat flux, effectively preclude a definitive estimate of c_h for the ISPOL floe, and for the analysis in the next section, we revert to a value inferred from previous measurements: $c_h = 0.0057$.

The bulk coefficient relates heat flux to the departure of mixed-layer temperature from freezing. This is not the same as the difference between far-field temperature and temperature at the ice/ocean interface, because salinity also varies near the boundary. From the "three-equation" description of heat and salt flux at the interface (e.g., Notz et al., 2003), we use exchange coefficients: $\alpha_T = 0.0095$ with $\alpha_T/\alpha_S = 30$ for the modeling results in Section 5. This combination approaches $c_h = 0.0057$ asymptotically for low heat flux values.

5. ISPOL ice/ocean interface and upper-ocean turbulence parameters

The steady LTC model provides a means of estimating interface fluxes and upper-ocean turbulence parameters representative of the ISPOL floe for the duration of its drift. To this end, the model was solved for every 3-h data average for which the relative current at 20 m depth exceeded $0.03\,m\,s^{-1}$. Temperature and salinity profiles were estimated by first interpolating between adjacent ship profiles (typically taken twice per day), then adjusting each by a constant offset so that the interpolated mixed-layer values agreed with the actual values measured at the mast TIC levels. We consider the most representative model estimate to be that based on $z_0 = 0.04$ m, following the analysis in Section 4.2.

Modeled-friction velocity is shown in Fig. 17, where daily mean values for $z_0 = 0.04$ m are indicated by the heavy dashed curve. The envelope indicates the range in daily values associated with a range in z_0 from 1 mm to 0.12 m. The limits suggest how the stress might vary across the floe depending on the ice undersurface: e.g., when the overall friction velocity (based on $z_0 = 0.04$ m) is $0.01\,m\,s^{-1}$, for smooth ice ($z_0 = 1$ mm), the effective u_{*0} would be about half as large. The mean representative modeled value for u_{*0} is $7.6\,mm\,s^{-1}$ (Table 2). When the

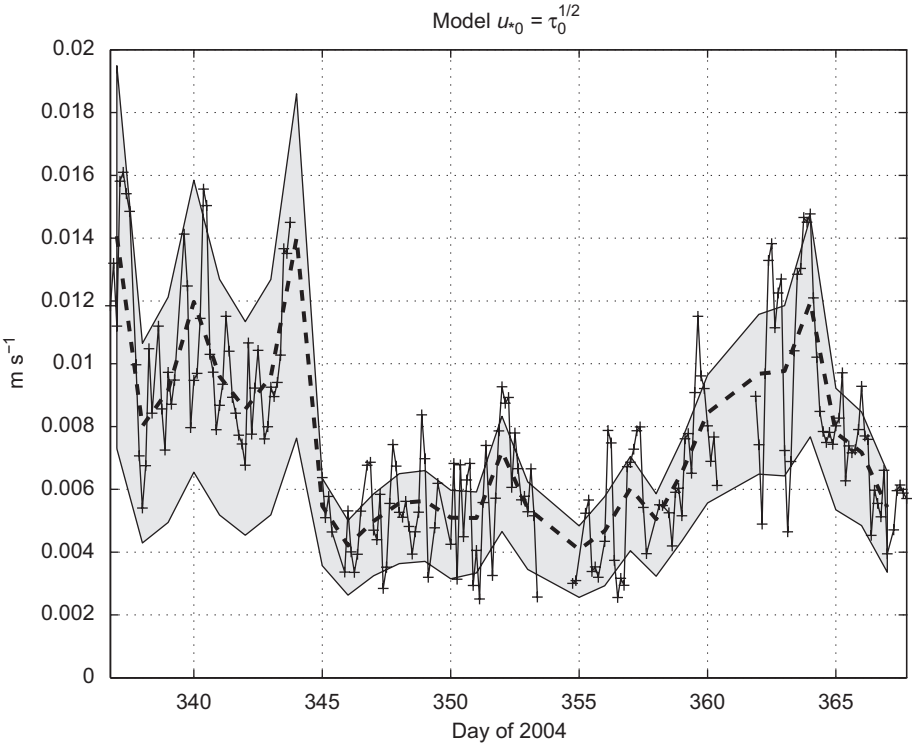

Fig. 17. Modeled interface friction speed plus symbols indicate values for every 3 h model realization when the relative current speed at 20 m equaled or exceeded $0.03\,m\,s^{-1}$, for the model with $z_0 = 0.04$ m. The heavy dashed curve connects daily average values. The gray filled region indicates the range of daily average values corresponding to models with the smoothest z_0 (1 mm, lowest values) to the roughest z_0 (0.12 m, highest values).

measured values at TIC 2 are extrapolated to the surface assuming complex exponential attenuation with distance (McPhee and Martinson, 1994), the mean value for u_{*0} from the Reynolds stress measurements (for current speeds $>0.03\,\mathrm{m\,s^{-1}}$) is $7.3\,\mathrm{mm\,s^{-1}}$. In other words, the measurements of momentum flux from the 4 m level at OT-I appear to represent the overall floe reasonably well (Fig. 18).

Interfacial heat flux inferred from the model (Fig. 17) responds to both u_{*0} and δT, as illustrated by the peak in H_f following day 350. Although stress during this period is relatively weak (Fig. 6), temperature elevation is high (Fig. 7B) resulting in large heat flux. Mean values for the entire drift (for relative currents exceeding $0.03\,\mathrm{m\,s^{-1}}$) are listed in Table 2. Closely related is the ice ablation rate $\dot{h}$, assuming that all of the heat exchange at the interface goes to melting. By this estimate the overall bottom ablation over the month-long drift would amount to roughly 14 cm. For the smoother ice ($z_0 = 1$ mm), the estimate is closer to 9 cm. Because very low current speeds were neglected in the modeling, these values would somewhat overestimate melt.

The last two columns of Table 2 are estimates of salinity flux at the interface, and associated buoyancy flux (thermal expansion is considered, but is negligible at these temperatures). Considering that the covariance calculations for salinity flux (Fig. 6) probably represent only half to three-quarters of the actual flux (because of the filtering affect of the standard conductivity meters), the mean values observed during OT-I are not so different from the modeling results of Table 2. (*Downward* fluxes during OT-II cannot be explained by the simple modeling.) The decrease in mixed-layer salinity evident in Fig. 6 also suggests the influence of meltwater. To examine this correspondence, we considered the vertically integrated salt conservation equation

$$\frac{\partial}{\partial t}\int_{-100}^{0}(S - S_{100})\mathrm{d}z = \frac{\partial \Delta_{\mathrm{salt}}}{\partial t} \approx -\left\langle w'S'\right\rangle_0 \tag{5}$$

where we used the change in salt content relative to the 100 m level, assuming that changes at 100 m are representative of horizontal advective changes in the water column above that level. The left hand side of (5) was approximated

Table 2
Mean modeled interface parameters

Model z_0 (m)	$\overline{u_{*0}}$ ($\mathrm{mm\,s^{-1}}$)	$\overline{H_{f0}}$ ($\mathrm{W\,m^{-2}}$)	$\dot{h}$ ($\mathrm{mm\,d^{-1}}$)	$\overline{\langle w'S'\rangle_0}$ ($\mathrm{psu\,m\,s^{-1}} \times 10^6$)	$\overline{\langle w'b'\rangle_0}$ ($\mathrm{W\,kg^{-1}} \times 10^8$)
0.040	7.6	15.0	4.7	1.51	1.09
0.001	4.6	9.3	2.9	0.93	0.67
0.120	9.4	18.0	5.6	1.81	1.30

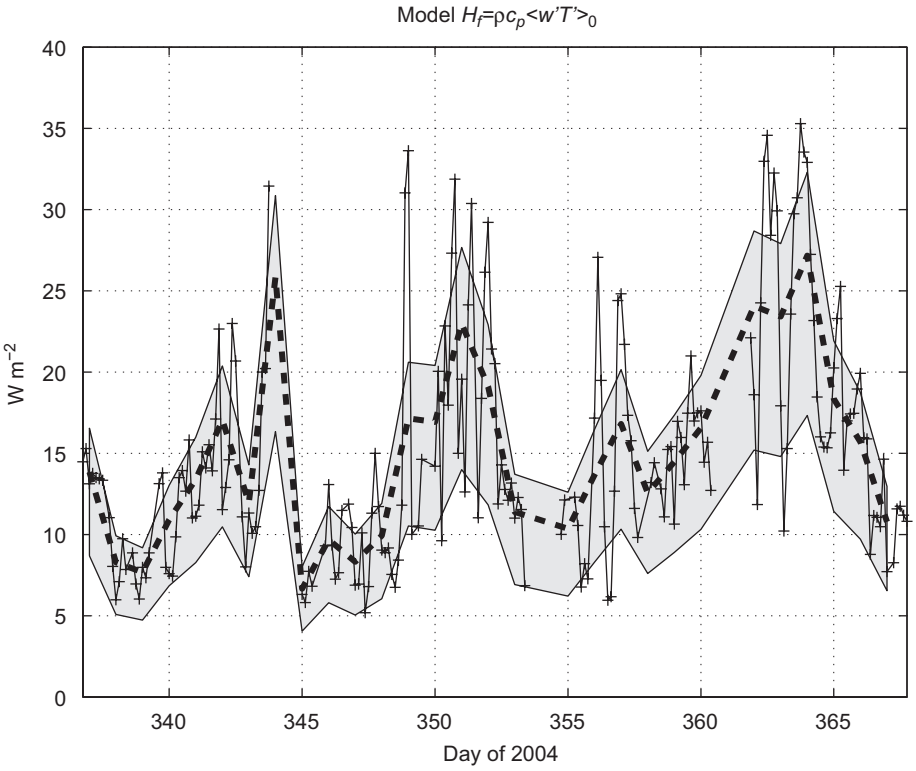

Fig. 18. Same as Fig. 17, except modeled interface heat flux.

by performing the integral numerically for each ship station, then calculating the slope of a regression of Δ_{salt} with time. For the model period, the slope was $-0.097\,\mathrm{psu\,m\,d^{-1}}$, which implies surface salinity flux of about $1.1\,\mathrm{psu\,m\,s^{-1}}$. This crude estimate is not unlike the values listed in Table 2, and suggests that melting could indeed account for the observed decrease in surface salinity.

The downward salinity flux observed during OT-II (Fig. 11D), consistent with observations that salinity at 1 m was slightly higher than at 3 m, cannot be explained by the modeling. A possible source could be leaching of high-salinity brine as the ice column warmed, but arguing against this interpretation is that the downward flux increased with increasing depth. An alternative explanation is a shadowing effect of the pressure ridge that was often "upstream" from OT-II (a typical situation is depicted in Fig. 14B). In this case, fluid having crossed the floe NE of the ridge would have been freshened by melting more than fluid protected in the wake of the keel, setting up a positive vertical gradient in salinity and associated downward salinity flux.

The modeled interface buoyancy flux (Fig. 19B) demonstrates that buoyancy was rarely important in the near boundary turbulence at ISPOL. Taking, for example, the representative mean values from Table 2, the Obukhov length based on mean interface quantities:

$$L_0 = \frac{u_{*_0}^3}{\kappa\langle w'b'\rangle_0} \tag{6}$$

is about 100 m (ranging from 36 to 160 m for the extreme values). In general, the importance of buoyancy production relative to shear production in the turbulent kinetic energy equation may be expressed as a fraction $-\lambda/L_0$ in the well-mixed layer. Comparison of the mean L_0 values with the λ estimates of Fig. 13 shows that this ratio is nearly always very small; i.e. that the stabilizing impact of meltwater is relatively unimportant at the measurement levels. It *is* important in determining the depth of the mixing, hence, where the seasonal pycnocline forms in response to melting.

The final modeling results to consider are estimates of eddy viscosity, K_m. By Reynolds analogy, the eddy diffusivities of scalar variables (heat, salt, nutrients) in a fully turbulent flow will be similar to the eddy viscosity. Fig. 20 shows K_m in two ways: at the fixed 2 m (from the interface) level, and as the maximum value in the boundary layer. Thus, for example, if the interest is turbulent exchange of nutrients very close to the interface, specifying eddy diffusivity to vary linearly with depth from the interface to the value of K_m at 2 m would provide a reasonable approach.

6. Summary and discussion

6.1. Ice drift and upper-ocean currents

Net ice drift for ISPOL was northward with mean velocity of $-0.015+i*0.017\,\mathrm{m\,s^{-1}}$ during Drift 1 and

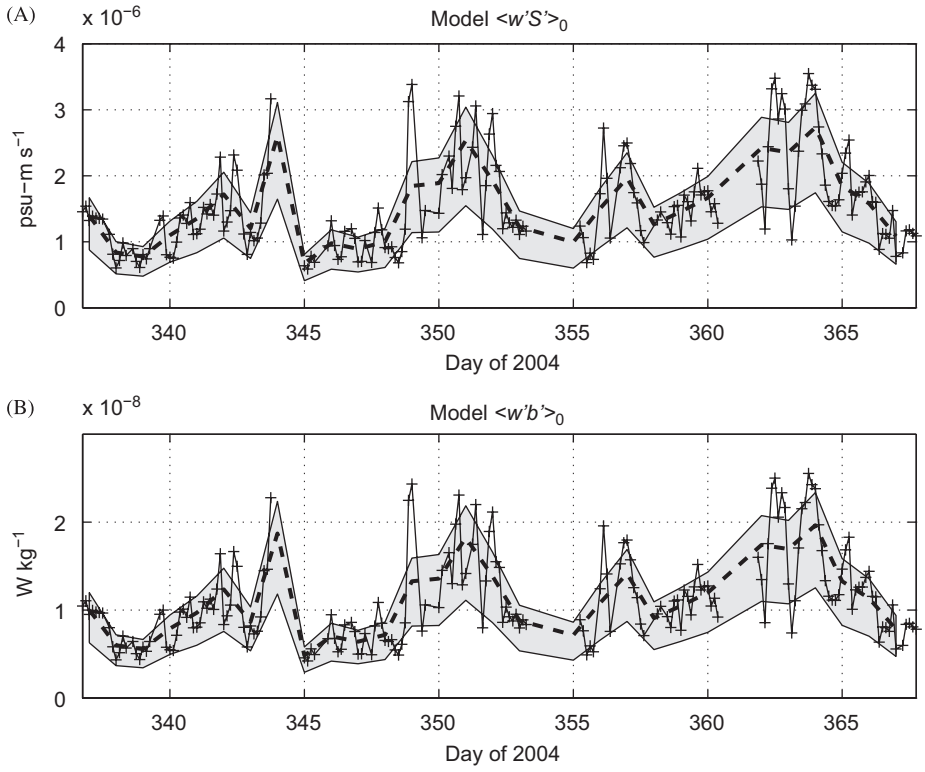

Fig. 19. (A) Modeled interface salinity flux, assuming that there is no heat conduction in the ice column, and that ice salinity is 4 psu and (B) modeled buoyancy flux.

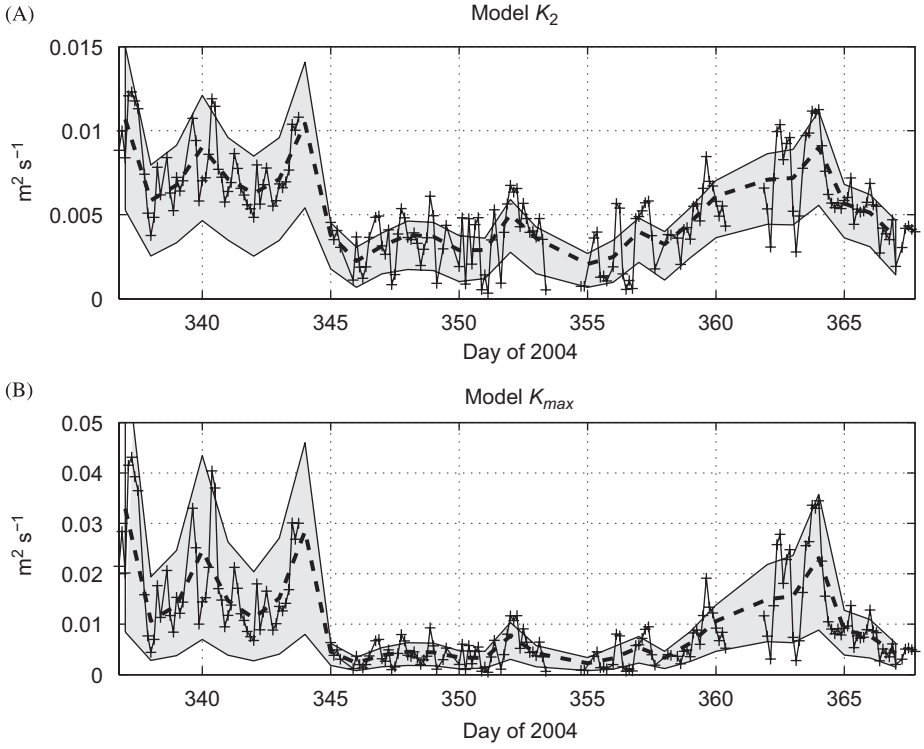

Fig. 20. Modeled eddy viscosity at the 2 m level (A) and the maximum value in the mixed layer (B).

$0.015 + i*0.075\,m\,s^{-1}$ during Drift 2. RMS ice speed was dominated by a mixed-diurnal/semidiurnal tide with the diurnal component larger by about 60%. The correlation between wind and ice drift was lower than typically found in multiyear ice in the Arctic during summer, with a mean ratio of ice drift speed (after removing tidal motion) to wind speed of about 1.5%. For comparison, during June at the SHEBA station on multiyear pack ice in the Arctic, the ratio was over 2% (McPhee, 2002), and for winter first-year ice in the eastern Weddell during the Antarctic Zone Flux Experiment in July, 1994, the average ratio approached 4% (McPhee et al., 1996), reflecting a much smoother ice underside. It appears that tidal and internal ice forcing were often as important as wind.

On short time scales, velocity profiles measured relative to the drifting ice with the 500-kHz ADP nearly always indicated leftward backing of the current vector with depth, a consequence of Coriolis (Ekman) turning in the upper ocean. A mean non-dimensional current hodograph, formed from the complex ratios of horizontal currents at fixed levels relative to the 30-m level (Fig. 5), demonstrated a convincing Ekman spiral in the upper ocean beneath a thin, high-shear surface layer, consistent with spirals observed under drifting sea ice in the Arctic (e.g., Hunkins, 1966).

6.2. Turbulent stress

Measured turbulent stress typically increased with distance from the interface, probably indicating increasing horizontal fetch radius encompassing larger roughness elements upstream from the measurement site. At both OT-I and OT-II, ice in the immediate vicinity of the turbulence mast(s) was smooth, but in both cases there were significant topographic features within ranges where their generated turbulence would be sensed by the lower TICs. This was particularly evident at OT-II, where surface roughness inferred from turbulence and mean flow measurements at 1 and 3 m differed by almost two orders of magnitude. In order to assess momentum transfer typical of the entire floe, a novel modeling approach was utilized that optimizes comparison between modeled and observed angular shear between fixed levels over a range of z_0 values. A model with $z_0 = 0.04$ m matched the current shear observations reasonably well. This value agreed with the estimate made directly from the 4 m level at OT-I by two methods, and falls about midway in the range of under-ice roughness inferred for multiyear pack ice in the Arctic (including ice in the marginal ice zone), as summarized, e.g., by McPhee (1990, Table 6.1).

Over the entire drift, the modeled interface friction speed, u_{*0}, was $7.6\,mm\,s^{-1}$; while u_{*0} at OT-I estimated by extrapolating the turbulent stress at 4 m to the interface, was $7.3\,mm\,s^{-1}$. The secular development of undersurface stress at ISPOL appeared to follow the spring-neap tidal cycle during the 1-month project. In this respect, the regime was somewhat analogous to a late winter project north of Yermak Plateau in the 1989 (CEAREX) during which under-ice stress was dominated by (stronger) tidal currents (McPhee, 1992). Both cases are exceptions to the general

rule that wind provides the main mechanical forcing for pack ice, especially during summer.

6.3. Ocean heat and salt flux

When solar radiation heats the water column through open leads or thin ice, energy absorbed near the surface is mixed downward by turbulence. McPhee and Stanton (1996) reported, for example, downward heat flux of $-70\,W\,m^{-2}$ at mid-day in the Arctic-mixed layer at the edge of a freezing lead in early April, even though air temperature was $-30\,^{\circ}C$ and ice was freezing rapidly. In June at the SHEBA station in 1998, there was a clear diurnal cycle in turbulent heat flux and mixed-layer temperature (McPhee et al., 2001).

T', w covariance statistics from ISPOL revealed a complex boundary layer thermal structure in which heat flux was alternately positive (up) or negative (down), sometimes changing sign across the span of the mast. Although there were times at ISPOL when the large downward fluxes appeared to coincide with solar zenith, there was no consistent cycle in measurements from OT-I. At OT-II, heat flux was generally upward, with a more regular pattern of rise in δT and heat flux magnitude in the afternoon (Fig. 8D). Besides direct vertical mixing of solar energy absorbed near the surface, downward heat flux also can result from relatively warmer water under-running cold. Plausible examples of both phenomena were evident during ISPOL, where measured heat flux appeared to depend on solar angle and relative fetch from open water or thin ice. The largest heat flux observed was downward ($-71\,W\,m^{-2}$) at 2 m in the afternoon (local) of day 356 (the summer solstice), when relative flow approached directly from an open lead about 70 m away.

Modeled interface heat flux, based on the overall momentum exchange and measured upper-ocean temperature, increased from about $10\,W\,m^{-2}$ early in December to about $25\,W\,m^{-2}$ by day 364; however, there was significant variability depending on both changes in u_{*0} and δT. These values are comparable to estimates for June in the Arctic from manned stations and drifting buoys (McPhee et al., 2003; Krishfield and Perovich, 2005).

Given the representative mean-modeled-heat flux of $15\,W\,m^{-2}$ (Table 2), an upper limit on bottom ablation integrated over all ice thicknesses would be around 15 cm for the entire drift. For smoother ($z_0 = 1$ mm) ice the maximum ablation would be about 9 cm. This assumes that all of the heat transfer at the interface goes to melting.

S', w covariance indicated predominantly upward salinity flux at OT-I, consistent with melting. If adjusted upward to account for the filtering effect of the ducted SBE 04 conductivity cells, mean values of $\overline{\langle w'S'\rangle}$ were consistent with modeled-interface salinity flux (1.5×10^{-6} psu m s^{-1}). Both were of the same order as a crude estimate derived from decreases in salt content relative to the 100 m level (1.1×10^{-6} psu m s^{-1}). Buoyancy flux associated with the small values of salinity flux were never very important in the TKE balance at the measurement levels. The most likely source of downward salinity flux observed at OT-II was horizontal advection of water freshened by bottom melting across an "upstream" pressure ridge keel.

6.4. Turbulence scales and eddy viscosity/diffusivity

The scale of turbulence in the upper few meters below the interface was investigated using a mixing length scale (λ) inversely proportional to the peak in the area-preserving variance spectra of vertical velocity. By showing an obvious trend of λ with increasing friction velocity, the results (Fig. 13) demonstrate convincingly that a dynamic scale proportional to u_*/f is often smaller than the geometric scale, $\kappa|z|$, even relatively close to the boundary, and thus determines the dominant turbulence scale. Despite appreciable scatter, Fig. 13 implies two important results. First, the data corroborate previous studies establishing a close link between the inverse wavenumber at the peak in the area-preserving vertical velocity variance spectrum and a fundamental turbulence scale (McPhee and Martinson, 1994). This makes it possible to estimate eddy viscosity or diffusivity at specific measurement levels in the boundary layer without directly invoking a comparison of turbulent flux and mean gradient. Second, the results underscore the importance of the planetary scale, as opposed to the geometric scale, for determining the dominant turbulence scale, even for measurements relatively close to the boundary. This is considerably different from a paradigm in which the turbulence scale is determined either by $\kappa|z|$, or by the extent of the mixed layer.

Eddy diffusivity of momentum (and by Reynolds analogy, eddy scalar diffusivity) is closely related to the mixing length scale, λ. In this work, a model based on similarity scaling of λ was combined with the observed non-dimensional current hodograph to infer characteristics deemed representative of the entire ISPOL floe (Section 5). For modeled conditions (20 m relative current $>= 0.03\,m\,s^{-1}$), maximum eddy viscosity in the mixed layer varied from about 4.5×10^{-4} to $4.3\times10^{-2}\,m^2\,s^{-1}$. Two meters from the ice it varied from 3.3×10^{-4} to $1.2\times10^{-2}\,m^2\,s^{-1}$.

Acknowledgments

We were privileged to be able to participate in the ISPOL project. Exemplary support from the officers and crew of the R.V. *Polarstern* is gratefully acknowledged, as was help from many in the science party making hydroholes, supplying power, deploying and recovering the turbulence mast, as well as providing stimulating company. Suggestions from two anonymous reviewers for improving the manuscript are appreciated.

This work was supported by the U.S. National Science Foundation, Office of Polar Programs, under Grants 0324043, 0337819, and 0337159.

References

Fer, I., McPhee, M.G., Sirevaag, A., 2004. Conditional statistics of the Reynolds stress in the underice boundary layer. Geophysical Research Letters 31, L15311 [doi:10.1029/2004GL020475].

Gordon, A.L., Ice Station Weddell Group of Principal Investigators and Chief Scientists, 1993. EOS, Transactions of the American Geophysical Union 74, 121–126.

Hellmer, H.H., Schröder, M., Haas, C., Dieckmann, G.S., 2008. The ISPOL drift experiment. Deep-Sea Research II, this issue [doi:10.1016/j.dsr2.2008.01.001].

Hunkins, K., 1966. Ekman drift currents in the Arctic ocean. Deep-Sea Research 13, 607–620.

Krishfield, R.A., Perovich, D.K., 2005. Spatial and temporal variability of oceanic heat flux to the Arctic ice pack. Journal of Geophysical Research 110, C07021 [doi:10.1029/2004JC002293].

McPhee, M.G., 1980. An analysis of pack ice drift in summer. In: Pritchard, R. (Ed.), Sea Ice Processes and Models. University of Washington Press, Seattle, pp. 62–75.

McPhee, M.G., 1981. An analytic similarity theory for the planetary boundary layer stabilized by surface buoyancy. Boundary-Layer Meteorology 21, 325–339.

McPhee, M.G., 1988. Analysis and prediction of short term ice drift, transactions of the ASME. Journal of Offshore Mechanics and Arctic Engineering 110, 94–100.

McPhee, M.G., 1990. Small scale processes. In: Smith, W. (Ed.), Polar Oceanography. Academic Press, San Diego, CA, pp. 287–334.

McPhee, M.G., 1992. Turbulent heat flux in the upper ocean under sea ice. Journal of Geophysical Research 97, 5365–5379.

McPhee, M.G., 1994. On the turbulent mixing length in the oceanic boundary layer. Journal of Physical Oceanography 24, 2014–2031.

McPhee, M.G., 1999. Scales of turbulence and parameterization of mixing in the ocean boundary layer. Journal of Marine Systems 21, 55–65.

McPhee, M.G., 2002. Turbulent stress a the ice/ocean interface and bottom surface hydraulic roughness during the SHEBA drift. Journal of Geophysical Research 107 (C10), 8037 [doi:10.1029/2000JC000633].

McPhee, M.G., 2004. A spectral technique for estimating turbulent stress, scalar flux magnitude, and eddy viscosity in the ocean boundary layer under pack ice. Journal of Physical Oceanography 34, 2180–2188.

McPhee, M.G., Martinson, D.G., 1994. Turbulent mixing under drifting pack ice in the Weddell Sea. Science 263, 218–221.

McPhee, M.G., Stanton, T.P., 1996. Turbulence in the statically unstable oceanic boundary layer under Arctic leads. Journal of Geophysical Research 101, 6409–6428.

McPhee, M.G., Maykut, G.A., Morison, J.H., 1987. Dynamics and thermodynamics of the ice/upper ocean system in the marginal ice zone of the Greenland Sea. Journal of Geophysical Research 92, 7017–7031.

McPhee, M.G., Ackley, S.F., Guest, P., Huber, B.A., Martinson, D.G., Morison, J.H., Muench, R.D., Padman, L., Stanton, T.P., 1996. The Antarctic zone flux experiment. Bulletin of the American Meteorological Society 77, 1221–1232.

McPhee, M.G., Kottmeier, C., Morison, J.H., 1999. Ocean heat flux in the central Weddell Sea in winter. Journal of Physical Oceanography 29, 1166–1179.

McPhee, M.G., Maykut, G.A., Bitz, C.M., Moritz, R.E., 2001. Early summer heating of the upper ocean in the vicinity of SHEBA. In: Proceedings of the Sixth Conference on Polar Meteorology and Oceanography, American Meteorological Society, 14–18 May 2001, San Diego, pp. 260–262.

McPhee, M.G., Kikuchi, T., Morison, J.H., Stanton, T.P., 2003. Ocean-to-ice heat flux at the north pole environmental observatory. Geophysical Research Letters 30 (24), 2274 [doi:10.1029/2003GL018580].

Morison, J.H., McPhee, M., 2001. Ice–ocean interaction. In: Steele, J., Thorpe, S., Turekian, K. (Eds.), Encyclopedia of Ocean Sciences. Academic Press, New York.

Notz, D., McPhee, M.G., Worster, M.G., Maykut, G.A., Schluenzen, K.H., Eicken, H., 2003. Impact of underwater-ice evolution on Arctic summer sea ice. Journal of Geophysical Research 108 (C7), 3223 [doi:10.1029/2001JC001173].

Perovich, D.K., Elder, B., 2002. Estimates of ocean heat flux at SHEBA. Geophysical Research Letters 29 (9) [doi:10.1029/2001GL014171].

Robertson, R., Padman, L., Levine, M.D., 1995. Fine structure, microstructure, and vertical mixing processes in the upper ocean in the western Weddell Sea. Journal of Geophysical Research 100, 18,503–18,517.

Rossby, C.-G., 1932. A generalization of the theory of the mixing length with application to atmospheric and oceanic turbulence. Massachusetts Institute of Technology Meteorological Papers 1 (4).

Thomas, D.N., Dieckmann, G.S. (Eds.), 2003. Sea Ice—An Introduction to its Physics, Chemistry, Biology and Geology. Blackwell Science, Oxford, UK.